



HAL
open science

Introducing ROMULUSC: a cosmological simulation of a galaxy cluster with an unprecedented resolution

M. Tremmel, T. R. Quinn, A. Ricarte, A. Babul, U. Chadayammuri, P. Natarajan, D. Nagai, A. Pontzen, M. Volonteri

► To cite this version:

M. Tremmel, T. R. Quinn, A. Ricarte, A. Babul, U. Chadayammuri, et al.. Introducing ROMULUSC: a cosmological simulation of a galaxy cluster with an unprecedented resolution. *Monthly Notices of the Royal Astronomical Society*, 2019, 483, pp.3336-3362. 10.1093/mnras/sty3336 . insu-03747944

HAL Id: insu-03747944

<https://insu.hal.science/insu-03747944>

Submitted on 9 Aug 2022

HAL is a multi-disciplinary open access archive for the deposit and dissemination of scientific research documents, whether they are published or not. The documents may come from teaching and research institutions in France or abroad, or from public or private research centers.

L'archive ouverte pluridisciplinaire **HAL**, est destinée au dépôt et à la diffusion de documents scientifiques de niveau recherche, publiés ou non, émanant des établissements d'enseignement et de recherche français ou étrangers, des laboratoires publics ou privés.

Introducing ROMULUSC: a cosmological simulation of a galaxy cluster with an unprecedented resolution

M. Tremmel,¹★ T. R. Quinn,² A. Ricarte,³ A. Babul,⁴ U. Chadayammuri,³
P. Natarajan,³ D. Nagai,^{1,3,5} A. Pontzen⁶ and M. Volonteri⁷

¹Physics Department, Yale Center for Astronomy & Astrophysics, PO Box 208120, New Haven, CT 06520, USA

²Astronomy Department, University of Washington, Box 351580, Seattle, WA 98195-1580, USA

³Department of Astronomy, Yale University, New Haven, CT 06511, USA

⁴Department of Physics and Astronomy, University of Victoria, 3800 Finnerty Road, Victoria, BC V8P 1A1, Canada

⁵Department of Physics, Yale University, New Haven, CT 06520, USA

⁶Department of Physics and Astronomy, University College London, Gower Street, London WC1E 6BT, UK

⁷Sorbonne Universit s, UPMC Univ Paris 6 et CNRS, UMR 7095, Institut d’Astrophysique de Paris, 98 bis bd Arago, F-75014 Paris, France

Accepted 2018 November 27. Received 2018 November 26; in original form 2018 June 4

ABSTRACT

We present the first results from ROMULUSC, the highest resolution cosmological hydrodynamic simulation of a galaxy cluster run to date. ROMULUSC, a zoom-in simulation of a halo with $z = 0$ mass $10^{14} M_{\odot}$, is run with the same sub-grid physics and resolution as ROMULUS25. With unprecedented mass and spatial resolution, ROMULUSC represents a unique opportunity to study the evolution of galaxies in dense environments down to dwarf masses. We demonstrate that ROMULUSC results in an intracluster medium consistent with observations. The star formation history and stellar mass of the brightest cluster galaxy (BCG) is consistent with observations and abundance matching results, indicating that our sub-grid models, optimized only to reproduce observations of field dwarf and Milky Way mass galaxies, are able to produce reasonable galaxy masses and star formation histories in much higher mass systems. Feedback from supermassive black holes (SMBHs) regulates star formation by driving large-scale, collimated outflows that coexist with a low-entropy core. We find that non-BCG cluster member galaxies are substantially quenched compared to the field down to dwarf galaxy masses and, at low masses, quenching is seen to have no dependence on mass or distance from the cluster centre. This enhanced quenched population extends beyond R_{200} and is in place at high redshift. Similarly, we predict that an SMBH activity is significantly suppressed within clusters outside of the BCG, but show how the effect could be lost when only focusing on the brightest active galactic nucleus in the most massive galaxies.

Key words: galaxies: clusters: general – galaxies: clusters: intracluster medium – galaxies: dwarf – galaxies: evolution – quasars: supermassive black holes.

1 INTRODUCTION

Galaxy clusters are the most massive, and recently assembled structures in the Universe and their dense environments offer an interesting astrophysical laboratory to test our current theories of galaxy evolution. The setting of a cluster in particular enables us to probe the dynamical processes that transform galaxies, and the interactions with the environment that shape their evolution. The modulation of star formation in cluster galaxies has been a subject of great interest as current observations suggest that star formation in these galaxies is quenched more often compared to isolated galaxies in the field

(e.g. Weinmann et al. 2006; Geha et al. 2012; Wetzel, Tinker & Conroy 2012; Wetzel et al. 2013; Haines et al. 2013, 2015). The truncation of star formation in cluster galaxies is thought to be a consequence of interactions with the intracluster medium (ICM) via processes such as ram pressure stripping (e.g. Chung et al. 2007; Merluzzi et al. 2013), ‘strangulation’ (e.g. van den Bosch et al. 2008; Maier et al. 2016), whereby the galaxy is starved of its gas reservoir that is not replenished due to the hot environment, or a combination of both (Murakami & Babul 1999; Bah  & McCarthy 2015). Additionally, interactions with other cluster member galaxies through either mergers or fly-by events (Moore et al. 1996; Moore, Lake & Katz 1998; Moore et al. 1999) may also play an important role in altering the star formation history and structural evolution of cluster member galaxies.

* E-mail: m.tremmel6@gmail.com

The central regions of galaxy clusters are also important as they often host the most massive galaxies in the Universe. Cluster samples selected via the Sunyaev–Zel’dovich effect show that ~ 30 per cent of clusters have cool cores (Andrade-Santos et al. 2017), meaning the central regions of their ICM have low entropy and short, sub-Gyr cooling times. The brightest cluster galaxies (BCGs) in these clusters, often located near the centre, have relatively low star formation rates (SFRs) compared with estimates based on gas cooling rates that predict upwards of $100s M_{\odot} \text{yr}^{-1}$ cooling flows (for reviews see Fabian 1994; Peterson & Fabian 2006). For BCGs, feedback from active galactic nuclei (AGNs) powered by accreting supermassive black holes (SMBHs) is thought to be the primary means of counteracting radiative cooling within the central region of the halo, thereby limiting cooling flows and star formation (e.g. Blanton et al. 2001; Babul et al. 2002; McCarthy et al. 2008; Gaspari, Brighenti & Temi 2012; Babul, Sharma & Reynolds 2013; Yang & Reynolds 2016; Prasad, Sharma & Babul 2017; Cielo et al. 2018a; Guo, Duan & Yuan 2018). This premise for BCGs is supported by observations of radio lobes and X-ray cavities (e.g. Boehringer et al. 1993; McNamara et al. 2000; Rafferty et al. 2006; O’Sullivan et al. 2012), often associated with jets (e.g. Fabian et al. 2002; Croston et al. 2011), which can both control the supply of gas in the inner regions of the halo as well as its ability to cool and form stars within the central galaxy. Thus, AGN feedback seems to be crucial not only for the evolution of the most massive galaxies in the Universe, but they may also affect the structure and properties of gas in the centres of clusters.

Multiwavelength observations of clusters, as well as gravitational lensing studies, are now able to extract more information about the structure of gas within clusters and the evolutionary history of their host galaxies (e.g. Mahdavi et al. 2008; Natarajan et al. 2009; Zhang et al. 2010; Mahdavi et al. 2013; Jauzac et al. 2015; Hitomi Collaboration et al. 2016; Smith et al. 2016). Numerical simulations are critical to understand the physical processes that shape the ICM and properties of cluster galaxies that are falling into assembling clusters. Modelling the physical scale of clusters presents a challenge for simulations due to the large dynamic range in the problem; the virial radii of clusters are on the scales of Mpc, while the physical processes of star formation, SMBH accretion, and feedback, as well as various hydrodynamic interactions, operate on kpc scales and far lower. Idealized simulations of galaxy clusters allow for very high resolution and can be useful for understanding the detailed interactions between SMBH feedback and the ICM (e.g. Ruzzkowski & Oh 2010; Gaspari et al. 2014; Li & Bryan 2014; Li et al. 2015; Prasad, Sharma & Babul 2015; Li, Ruzzkowski & Bryan 2017; Prasad et al. 2017; Cielo et al. 2018a,b; Prasad, Sharma & Babul 2018). However, these simulations lack the cosmological context, the history of hierarchical merging and gas accretion that will shape the more detailed structures of the ICM and transform the population of in-falling galaxies. Cosmological simulations can self-consistently model the evolution of a galaxy cluster within a larger scale, evolving environment starting from realistic initial conditions predicated by the standard cold dark matter model (e.g. Lewis et al. 2000). Gas and dark matter accumulate realistically and a population of galaxies bound to the larger cluster halo result naturally from these simulations. Due to their relative rarity, only large volume simulations have any galaxy clusters within them and, due to their size, even zoom-in simulations of clusters are computationally expensive. Recent large-scale cosmological simulations (see Table 1 for a summary of most recent efforts), often calibrated to reproduce observations of high-mass galaxies, have shown varying degrees

Table 1. Comparison with other recent cosmological hydrodynamic simulations that include haloes with $M_{\text{vir}} > 10^{14} M_{\odot}$ as well as full radiative hydrodynamics. M_{DM} and M_{gas} are dark matter and (average) gas particle masses, respectively. Note that many of the lower resolution simulations include dozens or hundreds of clusters while high-resolution simulations like ROMULUSC and TNG50 only have one.

Name	Spatial Res. ^a kpc	M_{DM} M_{\odot}	M_{gas} M_{\odot}
ROMULUSC	0.25	3.4×10^5	2.1×10^5
TNG300 ^b	1.5	7.9×10^7	7.4×10^6
TNG100 ^b	0.75	5.1×10^6	9.4×10^5
TNG50	0.3	4.4×10^5	8.5×10^4
(in progress ^c)	–	–	–
Horizon-AGN ^d	1	8.0×10^7	1.0×10^7
Magneticum ^{e,f}	10	1.3×10^{10}	2.9×10^9
Magneticum ^{e,f}	3.75	6.9×10^8	1.4×10^8
High res	–	–	–
Magneticum ^{e,f}	1.4	3.6×10^7	7.3×10^6
Ultra high res	–	–	–
C-EAGLE ^{g,h}	0.7	9.6×10^6	1.8×10^6
EAGLE ⁱ	0.7	9.6×10^6	1.8×10^6
(50, 100 Mpc)	–	–	–
Omega500 ^{j,k}	5.4	1.6×10^9	2.7×10^8
MACSIS ^l	5.9	5.7×10^9	1.0×10^9
BAHAMAS ^m	5.9	5.7×10^9	1.0×10^9
Rhapsody-G ⁿ	5.0	1.0×10^9	1.9×10^8

Notes. ^aPlummer equivalent values for gravitational softening presented if multiple given. If it varies with redshift, lowest values for low- z are presented. If it varies with particle type, dark matter values are used. When values are presented relative to h^{-1} , they are converted to kpc using the value of h corresponding to that simulation’s cosmology.

^bHighest resolution versions are shown. ^cMarinacci et al. (2018) ^dAs of the publishing of this paper. ^eDubois et al. (2014) ^fBocquet et al. (2016) ^gDolag, Komatsu & Sunyaev (2016) ^hBarnes et al. (2017a) ⁱBahé et al. (2017) ^jSchaye et al. (2015) ^kShirasaki, Lau & Nagai (2017) ^lNelson, Lau & Nagai (2014)

^mBarnes et al. (2017b) ⁿMcCarthy et al. (2017) ^oWu et al. (2015)

of success in reproducing and studying (among other things) BCG masses and star formation histories (e.g. Bahé et al. 2017; Barnes et al. 2017a; McCarthy et al. 2017; Pillepich et al. 2018; Ragone-Figueroa et al. 2018), baryonic content and properties of the ICM (e.g. Wu et al. 2015; Liang et al. 2016; Barnes et al. 2017a; Lau et al. 2017), AGN feedback, and SMBH growth (e.g. McCarthy et al. 2017; Bogdán et al. 2018), and the properties and evolution of cluster member galaxies (e.g. Elahi et al. 2016; Bahé et al. 2017; Pillepich et al. 2018; Zinger et al. 2018). While some simulations are now able to produce realistic BCG masses (e.g. Ragone-Figueroa et al. 2018), quenching star formation at later times often requires sub-grid models for AGN feedback that are explicitly tuned to increase feedback efficiency at higher masses (e.g. Weinberger et al. 2017). Such models can be very useful and are indeed necessary at lower resolution, but their nature makes them such that the interaction between SMBH feedback, halo gas, and star formation in BCGs cannot be considered a fully emergent property of the simulation. For studying cluster member galaxies, suites of dozens or hundreds of simulated clusters provide a large sample of massive cluster galaxies, but the limited resolution means that they will lack well-resolved galaxies with masses below that of the Milky Way.

In this paper, we present initial results from the ROMULUSC zoom-in cosmological simulation of a $1.5 \times 10^{14} M_{\odot}$ galaxy cluster

which is, to our knowledge, the highest resolution cosmological hydrodynamic simulation of a cluster run to $z = 0$ to date. Table 1 shows a list of other cosmological simulations that include at least one galaxy cluster of $M_{\text{vir}}(z = 0) > 10^{14} M_{\odot}$ to demonstrate how ROMULUSC represents a significant improvement in both spatial and mass resolution. It is important to note that ROMULUSC (as well as TNG50), only includes a single low-mass galaxy cluster while many of the other cosmological simulations produce dozens to hundreds of more massive haloes. While such a small sample size is certainly an important limitation, in this paper we focus on the interactions between the ICM and SMBH feedback and the evolution of cluster member galaxies, both of which require high resolution to study in detail. We show how ROMULUSC compares with various observational benchmarks in terms of several key cluster properties including those of the cluster gas and the BCG. The high resolution of this simulation allows us to resolve halo masses as low as $3 \times 10^9 M_{\odot}$ with $> 10^4$ particles and stellar masses as low as $10^7 M_{\odot}$ with > 100 star particles (though in this paper we make the conservative choice to focus on galaxy masses above $10^8 M_{\odot}$). ROMULUSC attains a maximum resolution for hydrodynamics of 70 pc, which has been shown in grid codes to be sufficient to resolve ram pressure stripping (Roediger et al. 2015), although a thorough convergence test was not done. This simulation represents the first in a planned suite of high-mass, high-resolution zoom-in simulations and provides a critical proof of concept for our sub-grid models of star formation and, in particular, SMBH physics, which have in no way been tuned to reproduce realistic galaxy clusters or BCGs.

In Section 2 we discuss the properties of the simulation, including relevant sub-grid physics models. In Section 3 we compare bulk properties of the gas in ROMULUSC to various observations. We examine the evolution of both the BCG and other cluster member galaxies in Section 4 and discuss our results in Section 5. A summary is presented in Section 6 and future work pertaining to this simulation and others planned is discussed in Section 7.

2 THE SIMULATION

ROMULUSC is a cosmological zoom-in simulation of a small galaxy cluster with $z = 0$ total mass of $1.5 \times 10^{14} M_{\odot}$. Haloes of this mass are generally only found in uniform volume simulations of at least 50^3Mpc^3 . Compared with all other modern cosmological simulations that include haloes of this mass, ROMULUSC has significantly higher mass and spatial resolution (see table 1) and includes, by $z = 0$, 227 galaxies within the virial radius with $M_{*} > 10^8 M_{\odot}$, all of which are well resolved with more than 10^4 particles per halo or more.

The initial conditions for ROMULUSC are extracted from a 50^3Mpc^3 uniform volume, DM-only simulation. The ‘zoom-in’ volume renormalization technique of Katz & White (1993) is used to resimulate the Lagrangian region associated with the most massive halo in the DM-only volume with full hydrodynamic treatment using the new Tree + SPH code CHANGA at higher resolution (Menon et al. 2015). Due to its ability to scale efficiently up to 500 000 cores, CHANGA is uniquely well suited to run such a large-scale, high-resolution simulation. CHANGA includes standard physics modules and physically motivated ingredients previously used in GASOLINE (Wadsley, Stadel & Quinn 2004; Wadsley, Veervalli & Couchman 2008; Wadsley, Keller & Quinn 2017) such as a cosmic UV background that includes self-shielding (Pontzen et al. 2008), star formation, ‘blastwave’ SN feedback (Stinson et al. 2006), and low-temperature metal cooling. CHANGA includes an

updated SPH implementation that eliminates artificial gas surface tension through the use of a geometric mean density in the SPH force expression (Ritchie & Thomas 2001; Governato et al. 2015; Menon et al. 2015), allowing for the accurate simulation of shearing flows with Kelvin–Helmholtz instabilities. Critical to this work, the simulation includes an updated implementation of turbulent diffusion (Wadsley et al. 2017), shown to be an important physical process for attaining realistic entropy profiles in galaxy cluster cores (Wadsley et al. 2008) as well as metal distributions in galaxies (Shen, Wadsley & Stinson 2010). Further, the simulations include a gradient-based shock detector, a time-dependent artificial viscosity, and an on-the-fly time-step adjustment system, the combination of which allows for a more realistic treatment of both weak and strong shocks (Wadsley et al. 2017).

ROMULUSC is run with the same hydrodynamics, sub-grid physics, resolution, and cosmology as the ROMULUS25 simulation (Tremmel et al. 2017). The cosmology is Λ CDM with cosmological parameter values following the most recent results from Planck ($\Omega_0 = 0.3086$, $\Lambda = 0.6914$, $h = 0.6777$, $\sigma_8 = 0.8288$; Planck Collaboration XIII 2016). The simulation has a Plummer equivalent force softening, ϵ_g , of 250 pc (a spline softening of 350 pc is used, which converges to a Newtonian force at $2\epsilon_g$). Unlike many similar cosmological runs, the dark matter distribution is *oversampled*, such that we simulate 3.375 times more dark matter particles than gas particles, resulting in a dark matter particle mass of $3.39 \times 10^5 M_{\odot}$ and gas particle mass of $2.12 \times 10^5 M_{\odot}$. This allows us to decrease numerical noise to more accurately track black hole dynamics (Tremmel et al. 2015). At this resolution, we confidently resolve haloes as small as $\sim 3 \times 10^9 M_{\odot}$ with at least 10^4 particles.

Fig. 1 shows the evolution of the stellar and gaseous components of the cluster over time. Fig. 2 shows the mass evolution of the cluster’s main progenitor halo, which reaches $10^{13} M_{\odot}$ by $z = 2$. Fig. 2 also shows the times for mergers (vertical dashed lines) of total mass ratio at least 1:10. The grey region represents an on-going merger of total mass ratio approximately 1:8 that starts at $z \sim 0.2$ and continues through $z = 0$. The galaxy involved in this merger can clearly be seen in the bottom left panel of Fig. 1. The galaxy has a stellar mass that is about half of that of the central BCG. We note that it may be possible that the lower mass galaxy could be mistaken as the BCG, though for simplicity we only consider the most massive galaxy to be the BCG in the following analysis. This is also the galaxy located at the potential minimum of the main progenitor branch of the main halo throughout the simulation. We also choose to ignore much of the evolution during this merger and instead focus on the cluster and BCG evolution when the cluster environment is comparatively relaxed prior to the merger event. As briefly discussed in Sections 3 and 4.1.2, the cluster would be classified as a cool-core cluster for much of the simulation, with a declining entropy profile down to $\sim 0.01 R_{200}$ and sub-Gyr cooling times in the core, but the merger destroys this structure, leaving the cluster in a non-cool-core state from $z \sim 0.2$ –0. Because the merger is ongoing at $z = 0$, we cannot be sure if this is a permanent transformation or a transient state due to the perturbation away from equilibrium (Poole et al. 2006, 2008). This merger event and the ensuing cool-core disruption will be explored in more detail in future work.

2.1 Star formation and feedback

Star formation and associated feedback from supernovae are crucial processes that require sub-grid models in cosmological simulations like ROMULUSC. As in previous work (Stinson et al. 2006) for runs at this resolution, star formation (SF) is regulated with parameters that

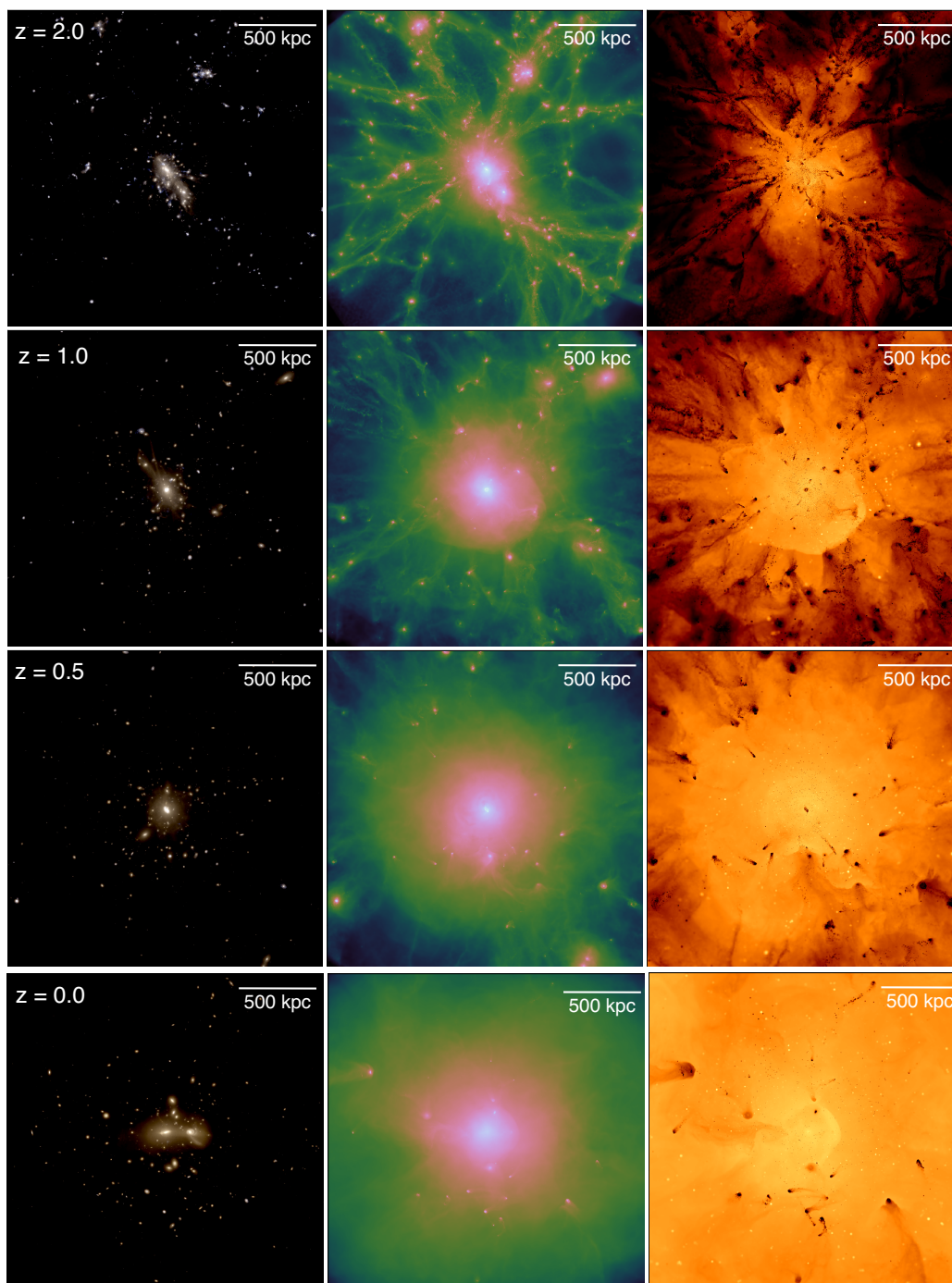


Figure 1. Evolution of gas and stars in ROMULUSC. Four snapshots of ROMULUSC taken (from the top) at $z = 2, 1, 0.5,$ and 0 showing stars (left-hand side), gas column density (middle), and gas temperature (right-hand side). The temperature is averaged along the line of sight and weighted by ρ^2 . All of the plots show the same physical region encompassing what will be R_{200} at $z = 0$ (the scales are also in physical units). The stars are shown in UVJ colours assuming a Kroupa IMF. The density ranges from $1 \times 10^{-5} \text{ g cm}^{-2}$ (blue/black) to 0.1 g cm^{-2} (pink/white). The temperature ranges from $5 \times 10^4 \text{ K}$ (black) to $5 \times 10^8 \text{ K}$ (yellow). At early times there are a lot of cold gas filaments penetrating the halo, which triggers more star formation in cluster galaxies. At later times, the halo is massive enough to prevent such filaments from penetrating far into the halo. Ram pressure stripping is evident in the extended tails of cold gas in the cluster galaxies. At $z = 0$ there are two galaxies interacting near the centre. The less massive of the two, which makes its first pericentre passage into the centre of the cluster around $z = 0.17$, is half the stellar mass of the BCG and comes from a halo one eighth the mass of the main halo.

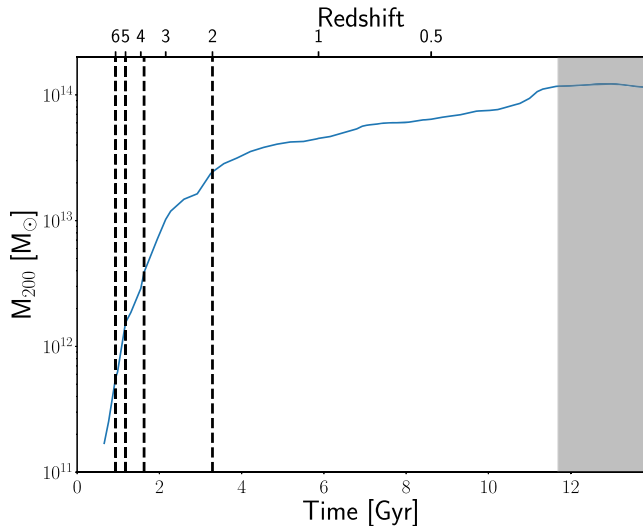


Figure 2. Growth of the ROMULUS cluster. The growth in halo mass of ROMULUS’s main progenitor over cosmic time. By $z \sim 2$ the main progenitor to ROMULUS is as massive as the most massive halo at $z = 0$ in our uniform volume simulation, ROMULUS25. Thus, ROMULUS represents a unique environment in which to examine galaxy evolution and an important addition to our simulation suite. Mergers of total mass ratio 1:10 or higher are shown as vertical dashed lines. The grey band represents the ongoing merger starting around $z = 0.17$, which has a 1:8 total mass ratio and a 1:2 stellar mass ratio. In some of our analysis we will ignore the time period associated with this merger.

encode star formation efficiency in dense gas, the coupling of SNe to the ISM, and the physical conditions required for star formation:

(i) the normalization of the SF efficiency, $c_{\star} = 0.15$, and formation time-scale, $\Delta t = 10^6$ yr, are both used to calculate the probability of creating a star particle from a gas particle that has a dynamical time t_{dyn}

$$p = \frac{m_{\text{gas}}}{m_{\text{star}}} (1 - e^{-c_{\star} \Delta t / t_{\text{dyn}}}), \quad (1)$$

(ii) The fraction of SNe energy that is coupled to the ISM, $\epsilon_{\text{SN}} = 0.75$

(iii) the minimum density, $n_{\star} = 0.2 \text{ cm}^{-3}$, and maximum temperature, $T_{\star} = 10^4$ K, thresholds beyond which cold gas is allowed to form stars.

SN feedback is included via the ‘blastwave’ implementation (Stinson et al. 2006), and gas cooling is regulated by metal abundance as in Guedes et al. (2011) as well as SPH hydrodynamics and both thermal and metal diffusion as described in Shen et al. (2010) and Governato et al. (2015). We assume a Kroupa IMF (Kroupa 2001) with associated metal yields.

An important limitation of the ROMULUS simulations in modelling higher mass haloes is that they only include low-temperature metal cooling rather than a full implementation of metal line cooling, a major coolant for higher temperature gas in groups and clusters. Metal line cooling has been shown to affect the accretion of gas on to galaxies in the centres of massive haloes, though feedback from AGN is also critically important in regulating this process (van de Voort et al. 2011b). The reason to exclude metal line cooling was made based on results from Christensen et al. (2014), who found that the inclusion of metal cooling without molecular hydrogen physics and more detailed models of star formation resulted

in overcooling in galaxies. The higher temperature metal cooling requires that a true multiphase interstellar medium (ISM) is maintained to keep the cooling at intermediate temperatures from running away. This means that higher resolution and clumpy star formation from molecular hydrogen is needed. Due to the scale of the ROMULUS simulations such resolution criteria are not met and so metal cooling is not implemented.

One possible solution to the overcooling problem would be to boost supernova feedback efficiency (e.g. Dalla Vecchia & Schaye 2012; Shen et al. 2012; Schaye et al. 2015; Sokołowska et al. 2016; Sokołowska et al. 2018), but this will not necessarily provide a realistic ISM or CGM/ICM. Sokołowska et al. (2016) showed for zoom-in simulations of Milky Way-like galaxies that the inclusion of metal-line cooling and enhanced SN feedback, while producing a reasonable stellar mass, resulted in unrealistic ISM and CGM properties compared to simulations without high-temperature metal cooling. Christensen et al. (2014) find that ISM models that include both metal lines and H_2 physics result in galaxies with star formation histories and outflow rates more similar to primordial cooling runs than to simulations with metal lines and no H_2 . Another solution would be to only allow metal cooling in diffuse gas that is less likely to be multiphase, but determining an arbitrary threshold where unresolved multiphase structure exists is difficult, particularly at the boundary of the ISM and the CGM/ICM where the effects will be most important for galaxy evolution, a major focus of the ROMULUS simulations. Given the severe flaws in both of these solutions, we choose to not include metal line cooling in ROMULUS.

2.2 Black hole physics

One of the major improvements in the ROMULUS simulations compared to previous work is the more sophisticated modelling of the seeding, fuelling, feedback, and dynamics of black holes. Below we summarize the model used in this work focusing particularly on the most relevant aspect: feedback from growing SMBHs. For more details regarding the model and the parameter optimization used to set their free parameters the reader is referred to Tremmel et al. (2017).

2.2.1 SMBH seeding

SMBHs are seeded in the simulation based on gas properties, forming in rapidly collapsing, low metallicity regions in the early Universe. The goal is to better approximate theoretical models of SMBH formation where they form at high redshift in lower mass, atomic cooling haloes (e.g. Schneider et al. 2002; Bromm & Loeb 2003; Lodato & Natarajan 2006). We isolate pristine gas particles (metallicity $< 3 \times 10^{-4}$) that have reached densities 15 times higher than what is required by our star formation prescription without forming a star or cooling beyond 9.5×10^3 K (just below the temperature threshold used for star formation, 10^4 K). These regions are collapsing on time-scales much shorter than the cooling and star formation time-scales and are meant to approximate the regions that would result in SMBHs of mass $> 10^6 M_{\odot}$, regardless of the details of their formation mechanism. The initial seed SMBH mass is set to $10^6 M_{\odot}$ and is justified by our choice of formation criteria, which would produce black holes that are able to attain higher masses quickly, as there is a lot of dense, collapsing gas nearby that is unlikely to form stars. Tremmel et al. (2017) show how this method forms most SMBHs within the first Gyr of the simulation, compared

with the later seeding times inherent to more common approaches that seed SMBHs based on halo mass thresholds (e.g. Springel, Di Matteo & Hernquist 2005; Di Matteo et al. 2008; Genel et al. 2014; Schaye et al. 2015). Unlike these other approaches, our model produces an evolving occupation fraction. At early times, small haloes ($M_{\text{vir}} \sim 10^{8-10} M_{\odot}$) host newly seeded SMBHs and the occupation fraction then evolves due to hierarchical merging. For example, in ROMULUS25 at $z = 5$ the SMBH occupation fraction of $\sim 10^{10} M_{\odot}$ haloes is ~ 60 per cent but at $z = 0$ the occupation fraction for haloes of this mass drops to ~ 10 per cent.

2.2.2 SMBH dynamics

We incorporate the dynamical friction sub-grid model presented in Tremmel et al. (2015) that permits the more accurate tracking of SMBH orbits within galaxies. The model approximates the unresolved dynamical friction that should act on SMBHs by integrating the Chandrasekar formula from the 90° deflection radius out to the gravitational softening length. Close encounters that should occur at this scale are important for dynamical friction, but are unresolved due to both the gravitational softening and limited mass resolution. This approach has been shown to produce a more realistic dynamical evolution of SMBHs at the resolution of ROMULUSC (Tremmel et al. 2015, 2018).

SMBH dynamics can be important in galaxy clusters since many mergers at high redshift will eventually make up the central galaxy. There are also many glancing encounters between cluster member galaxies (Moore et al. 1996; Moore et al. 1998, 1999). How SMBHs within galaxies respond to such perturbations can have an effect on their growth and feedback history and so it is important to follow their dynamics realistically. This includes their gradual sinking to halo centre resulting from a merger as well as becoming temporarily perturbed away from halo centre due to a merger or fly-by interaction. This dynamical evolution can also affect the ability for SMBHs to grow via SMBH mergers or accretion (Di Cintio et al. 2017; Tremmel et al. 2018). We refer the reader to Tremmel et al. (2015) for more details about the dynamical friction sub-grid model.

2.2.3 Accretion and feedback

Accretion of gas on to SMBHs is governed by a modified Bondi–Hoyle prescription, re-derived using the same energy balance argument as Bondi–Hoyle but including the additional angular momentum support present for rotating gas. Despite the fact that ROMULUSC has significantly higher mass and spatial resolution compared with other cosmological cluster simulations, the Bondi radius of even the most massive SMBHs remains unresolved. In the simulation, the properties of gas particles are defined by the average values smoothed over a kernel of typical size at least 10 per cent the gravitational softening, ε_g . However, because in reality dense, cool gas has a multiphase structure on scales well below our resolution limit, this will result in gas densities and temperatures that are systematically under- and overestimated, respectively, compared with what they should be nearby the SMBH. This will lead to artificially lower accretion rate estimates due to the failure of the simulation to resolve the multiphase nature of dense gas. We therefore follow Booth & Schaye (2009) and employ a density-dependent multiplicative boost factor to our modified Bondi–Hoyle accretion rate calculation in order to account for this unresolved multiphase structure and its impact on gas accretion on to SMBHs.

Taking both angular momentum and unresolved gas structure into account, the accretion equation has the following form:

$$\dot{M} = \alpha \pi (GM)^2 \rho \times \begin{cases} \frac{1}{(v_{\text{bulk}}^2 + c_s^2)^{3/2}} & \text{if } v_{\text{bulk}} > v_\theta \\ \frac{\varepsilon_s}{(v_\theta^2 + c_s^2)^2} & \text{if } v_{\text{bulk}} < v_\theta \end{cases}$$

$$\alpha = \begin{cases} \left(\frac{n}{n_{\text{th},*}}\right)^\beta & \text{if } n > n_* \\ 1 & \text{if } n < n_* \end{cases} \quad (2)$$

Values for density (ρ), number density (n), and sound speed (c_s) of gas near the SMBH are estimated from smoothing over the 32 nearest gas particles and accretion is not allowed to occur from gas particles farther than $4\varepsilon_g$ (1.4 kpc). The tangential velocity, v_θ , is derived from the *resolved* kinematics of nearby gas particles and compared to v_{bulk} , the overall bulk motion of the gas that already enters into the Bondi–Hoyle model. This bulk motion is taken to be the minimum relative velocity of the 32 nearest gas particles. When either the bulk motion or internal energy of the gas dominates over rotational motion, the accretion model reverts to the normal Bondi–Hoyle prescription. In both cases, we add the boost factor, α , calculated by comparing the number density of nearby gas particles to the threshold for star formation, n_* , defined in Section 2.1. For lower densities, we assume that the gas is not sufficiently multiphase to require such a boost, as in Booth & Schaye (2009). How much this boost increases with density is governed by β , a free parameter, which is set to 2.

An accreting SMBH converts a fraction of the accreted mass into energy that is transferred to nearby gas particles. This feedback efficiency is determined by two separate parameters: ε_r , the radiative efficiency, and ε_f , the efficiency of energy coupling to nearby gas. The overall feedback efficiency of the SMBH is the product of these two values. For the purposes of optimizing free parameters, we assume that ε_r is 0.1 and treat ε_f as a free parameter set to 0.02. It should be noted that ε_r and ε_f are not totally degenerate. The radiative efficiency is used to determine the Eddington limit, which we assume is the highest accretion rate attainable by any SMBH in the simulation.

Accretion and feedback are calculated during each SMBH time-step and are meant to represent the total amount of mass and feedback imparted during that time. While the SMBH is growing, thermal energy is transferred to the 32 nearest gas particles and they are not allowed to undergo cooling for a time equal to the SMBH’s time-step. *SMBHs are continuously placed on the lowest global time-step in the simulation.* For the majority of the simulation, this ends up being at most 10^5 yr and is more typically 10^3 – 10^4 yr. Further, gas particles within each SMBH’s smoothing region (i.e. the 32 closest particles) are forced to be on a time-step within a factor of 2 of the SMBH. These time-step criteria, as well as the brief cooling shut-off period, ensure (1) a more continuous sampling of accretion and feedback processes and (2) that the gas does not artificially radiate away the energy transferred by the SMBH due to limited spatial and time resolution.

2.2.4 Comparison with other implementations of feedback

Often, the choice to impart feedback through kinetic rather than thermal coupling is made due to numerical effects. Thermal energy is radiated away very easily by the dense gas that is generally near growing SMBHs. This is not physical, but rather the result of limited spatial, mass, and time resolution. When massive, dense gas particles are given a large amount of energy instantaneously and then allowed to cool based on their temperature and density properties over the course of their next time-step, they will invariably lose

that energy well before their internal properties are able to respond to the energy injection (Katz 1992). By forcing the SMBHs and surrounding gas particles to have small time-steps and by turning off cooling for a short time, we are able to better approximate a continuous transfer of energy between an accreting SMBH and the surrounding gas. This allows gas that is receiving feedback to expand and become buoyant, driving large-scale, thermally driven, collimated outflows (see Section 4.1).

Our adopted feedback model is empirically supported by velocity profiles of observed AGN-driven outflows, which are consistent with being energy conserving, rather than momentum conserving (Gaspari & Sądowski 2017). Gas that receives feedback on the smallest resolved scales of the simulation is really gas that has been entrained in an outflow initially driven by unresolved processes. Because energy is conserved in this outflow, it makes sense to inject it via thermal energy along with a cooling shutoff to ensure energy conservation. The outflow is then naturally driven by the hot, expanding gas affected by the feedback, similar to ‘blastwave’ SN feedback (Stinson et al. 2006).

Many simulations employ a two-mode feedback prescription (e.g. Sijacki et al. 2007; Dubois et al. 2012; Vogelsberger et al. 2013; Weinberger et al. 2017) whereby a transition occurs between a thermally driven mode of feedback during a radiatively efficient ‘quasar’ mode of SMBH activity to a radiatively inefficient ‘radio’ mode of SMBH activity, which captures momentum-driven feedback and is needed to reproduce the radio lobes observed in massive galaxies. In such models, the efficiency of feedback increases for high-mass galaxies/SMBHs, which is needed in order to effectively prevent overcooling. In effect, the main difference between these models and our own is (1) our overall feedback efficiency is held constant, (2) we always transfer energy thermally, and (3) feedback is implemented in the same way for all galaxies and does not change with redshift, SMBH mass, or galaxy mass.

The reasoning to impart kinetic feedback is supported by the existence of relativistic jets, often associated with radio ‘bubbles’ and X-ray cavities (e.g. Fabian et al. 2002; Croston et al. 2011). The kinetic power in such structures is thought to play a crucial role in balancing cooling flows in the centres of galaxy clusters (McNamara & Nulsen 2012). This process is generally modelled in idealized simulations by imparting momentum to gas within a region (usually a cylinder or bipolar cone) centred on the SMBH to approximate the directional momentum coupling of gas due to the presence of a jet (e.g. Cielo et al. 2014; Li & Bryan 2014; Prasad et al. 2015). Not only does such a method directly prescribe the momentum and morphology of the outflow on rather large scales, but it also assumes a direction of that momentum transfer. Cosmological simulations (and even idealized cluster simulations) do not have the resolution required to directly follow the spin of SMBHs and ROMULUSC is no exception, so the direction of a jet is purely a result of the sub-grid model assumptions. It has been shown that fixed direction jet heating is unable to reproduce observed cluster gas properties and cannot solve the overcooling problem (Vernaleo & Reynolds 2006; O’Neill & Jones 2010; Babul et al. 2013). For this reason, simulations that attempt to model this jet process often incorporate a changing direction, generally modelled as a precessing/re-orienting jet (Cielo et al. 2017, 2018b) or, as is often the case in cosmological simulations with relatively long time-steps, momentum transfer where nearby gas is given a radial kick equally in all directions (Weinberger et al. 2017).

How jets couple to the ISM and ICM is still an open question. While constraining the power within these bubbles/lobes from ob-

servations can be challenging, the fact that these lobes often encapsulate a power 10–1000 times that of the observed synchrotron radiation seems a relatively robust result [but see Snijs et al. (2018) for a potential exception], implying that much of the energy causing this structure likely resides in more massive particles (De Young 2006; Birzan et al. 2008; Hardcastle & Croston 2010). It is possible, therefore, that even with a relativistic jet the majority of feedback energy comes from gas entrained on smaller scales. The practical effect of a jet then would be to modulate the efficiency of feedback coupling to gas on ~ 100 pc scales. Over long periods of time, this would change how accretion itself regulates in systems dominated by radiatively inefficient accretion processes. This would affect the amount of SMBH accretion, but should only be a secondary effect in terms of the large-scale environmental impact of the feedback. Because it is not clear when a jet should or should not be active, given that the detailed physics of accretion are not followed in the simulation, we choose to ignore this effect and maintain a constant feedback efficiency rather than introduce additional free parameters. However, as is briefly discussed in Section 5.1, we do find evidence that higher feedback efficiencies may be required for high-mass galaxies/SMBHs.

In Section 4.2 we discuss how the interaction between AGN-driven outflows in our simulation and gas on both small (1–10 kpc) and large (10s–100s kpc) scales naturally causes an evolution in wind structure that overcomes the problems seen in fixed direction outflows implemented in idealized simulations. The fact that our model results in highly collimated outflows extending out to large scales shows that a kinetic feedback prescription is *not required* to produce such structures.

2.3 Free parameter optimization

As described in Tremmel et al. (2017), we use a novel approach for optimizing the free parameters involved in our sub-grid models for both stars and SMBHs and their respective feedback processes. To do this we ran a large set of zoom-in cosmological simulations of haloes with masses $10^{10.5}$, $10^{11.5}$, and $10^{12} M_{\odot}$ including full hydrodynamics, star formation, and SMBH physics. The simulations were all run at the same resolution of ROMULUSC and ROMULUS25. Each set of simulations was run using different parameters and graded against different $z = 0$ empirical scaling relations related to star formation efficiency, gas content, angular momentum, and black hole growth. From a total of 39 parameter realizations tested using these zoom-in simulations, we utilized an adapted Gaussian process Kriging technique to pinpoint regions in parameter space that create galaxies that most closely resemble the mean population at $z = 0$ and to determine when we had converged to the optimal choice [see appendix A of Tremmel et al. (2017) for more details]. This resulted in a complete set of sub-grid models governing star formation, stellar feedback, and SMBH accretion and feedback that are optimized to provide realistic $z = 0$ galaxies while maintaining predictive power at higher redshifts and high mass ($M_{\text{vir}} > 10^{12} M_{\odot}$). Tremmel et al. (2017) demonstrated how the parameters result in realistic SMBH and stellar masses for galaxies in haloes up to $10^{13} M_{\odot}$ as well as a realistic cosmic star formation and SMBH accretion histories out to high redshift for field galaxy populations. Importantly, this means that the parameters used in ROMULUSC were *in no way constrained to provide realistic results in terms of galaxy evolution in cluster environments*. The results presented in this paper are, therefore, purely a prediction of our model.

2.4 Halo and galaxy extraction

For all ROMULUSC simulations described in this work, haloes are extracted and catalogued using the Amiga Halo Finder (Knollmann & Knebe 2009). Haloes are defined based on all types of particles (dark matter, gas, and stars) and gravitational unbinding is performed. The centres of haloes are defined using a shrinking spheres approach (Power et al. 2003), which also consistently traces the centres of the central galaxies within each halo.

3 PROPERTIES AND STRUCTURE OF THE ICM IN ROMULUSC

In this section, we study the properties and structure of the gas within ROMULUSC and compare these with various observations. The temperature and entropy of cluster gas is determined by the structure of gas that collapses into the cluster to make up the ICM as well as further heating and cooling processes that take place within the cluster (e.g. radiative cooling, heating from AGN, and stellar feedback). It is also shaped by the processes of hierarchical merging and galaxy evolution occurring prior to and during cluster formation. Only a cosmological simulation naturally captures these different phases of evolution. Comparing the global properties and structure of the ICM in ROMULUSC is an important benchmark for determining how well our model for feedback, particularly that of AGN, is able to correctly predict ICM properties observed in cluster environments. We show that ROMULUSC reproduces empirical scaling relations, baryonic content, and average ICM profiles in observed clusters. This successful match to key physical properties is crucial and will allow us to use ROMULUSC and future simulations of this type to better understand the origin and evolution of the ICM as well as galaxy evolution within cluster environments.

In the following analysis, R_Δ is defined as the radius within which the average density is $\Delta \times \rho_{\text{crit}}$. A property such as M_Δ is then the mass within R_Δ . We also will show some results at both $z = 0$ and $z = 0.3$. This is because ROMULUSC undergoes a merger with a group at $z \sim 0.2$ that is still on going at $z = 0$, causing the cluster to be out of equilibrium. The detailed dynamical and hydrodynamical evolution of the cluster during this period will be the topic of future work and is beyond the scope of this paper. All results for ROMULUSC are given using 3D radii, though we confirm that this choice makes little difference were we to use projected quantities instead.

Current observations of gas in clusters rely on emission detectable in X-rays, so in this section we only consider gas from ROMULUSC that has temperatures above 10^6 K, or ~ 0.1 keV, consistent with the rough lower limits of Chandra’s observational sensitivity. Emission weighting is done by weighting each particle by its luminosity in the X-ray. To estimate this, we calculate the volume emissivity, ϵ_X , given by the following equations from Balogh, Babul & Patton (1999):

$$\epsilon_X = \frac{3}{2} \frac{\rho k_b T}{\mu m_h t_{\text{cool}}}$$

$$t_{\text{cool}} = 3.88 \times 10^{11} \mu m_h \frac{T^{0.5}}{\rho (1 + 5 \times 10^7 f_m/T)}. \quad (3)$$

The metallicity-dependent factor, f_m , is taken to be 1, consistent with solar metallicity. The results we present are not sensitive to this choice. The other factors, m_h , k_b , and T , are the mass of hydrogen, the Boltzmann constant, and temperature of the gas, respectively. We derive the value of μ directly for individual gas particles in the simulation based on their tracked metal abundances and ion content. We confirm this choice does not affect our results were we to assume

$\mu = 0.59$ for all gas particles. To get the luminosity of each particle, we multiply by its volume, where the volume of the i th particle is given by $V_i = m_i/\rho_i$, where m_i is the mass of the particle and ρ_i is its density.

Temperatures calculated within a given radius (i.e. T_{500}) are calculated excising the inner $0.15R_{500}$, consistent with observations (see Liang et al. 2016, and references therein). Specific entropy is calculated at a given radius using the widely accepted proxy, $S(r)$, related to the thermodynamic specific entropy by $ds \propto dlnS$ (Balogh et al. 1999). This value, which we shall refer to as ‘entropy’ hereafter, is given by

$$S(r) = \frac{k_b T_e(r)}{n_e r^{2/3}}. \quad (4)$$

The masses for the observed clusters are typically calculated using X-ray observations and assuming hydrostatic equilibrium. This has been found to underestimate the halo mass using both hydrodynamic simulations (Nagai, Vikhlinin & Kravtsov 2007) and lensing observations (Hoekstra et al. 2015). When presenting observations with X-ray-derived halo masses, we multiply the published masses by a factor of 1.3 to account for this bias. Nowhere are our conclusions sensitive to the inclusion of this correction value.

Fig. 3 shows the baryonic, hot gas, and stellar mass fractions within R_{500} for ROMULUSC plotted against a large sample of observed clusters and groups. In all cases, ROMULUSC is consistent with observations, though slightly on the high end of the scatter. This is an important result. As discussed in Section 4.1, the central galaxy is quenched by the presence of large-scale outflows driven by a central AGN. Such outflows can affect the ability for gas to cool on to the central BCG by either balancing the radiative cooling of the gas or by expelling it entirely. The fact that ROMULUSC results in realistic stellar and gas mass fractions means that star formation is suppressed without unrealistically evacuating large amounts of gas. This has been an issue in some cosmological simulations (Genel et al. 2014), where the solution has been to modify the nature of AGN feedback in massive systems (Weinberger et al. 2017). Our results shown here are similar to what has been found in other recent cosmological cluster simulations (e.g. Barnes et al. 2017a; Pillepich et al. 2018).

Fig. 4 plots the relationship between mass and the ICM temperature within R_{500} for observed groups and clusters, with the results from ROMULUSC overplotted as blue points. Here the temperature for ROMULUSC is taken as an average between the mass-weighted and emission-weighted temperatures, shown by Liang et al. (2016) to be a better approximation for the spectroscopic temperature that an observer would derive (Mazzotta et al. 2004; Vikhlinin 2006). We confirm that our results are insensitive to this choice. The results from ROMULUSC match the observed relationship well at both $z = 0$ and $z = 0.3$. In order to not include denser gas within substructure (see Zhuravleva et al. 2013), we only include gas with densities less than $500\rho_{\text{crit}}$. This value was arrived at empirically, as more strict cuts lower temperature estimates because they remove hot cluster gas outside $0.15R_{500}$ and less strict cuts also lower temperature estimates because they miss dense substructure. Our results are insensitive to the exact choice of density threshold, in part because emission weighting is only used when the values are averaged with mass-weighted values. For future, more detailed analysis of the ICM a more careful approach will be used to remove substructure gas. However, for the purposes of this paper the simple, single density cut approach is sufficient.

Fig. 5 plots the entropy calculated within 1 kpc wide annuli at both R_{500} and R_{2500} for observed groups and clusters with the re-

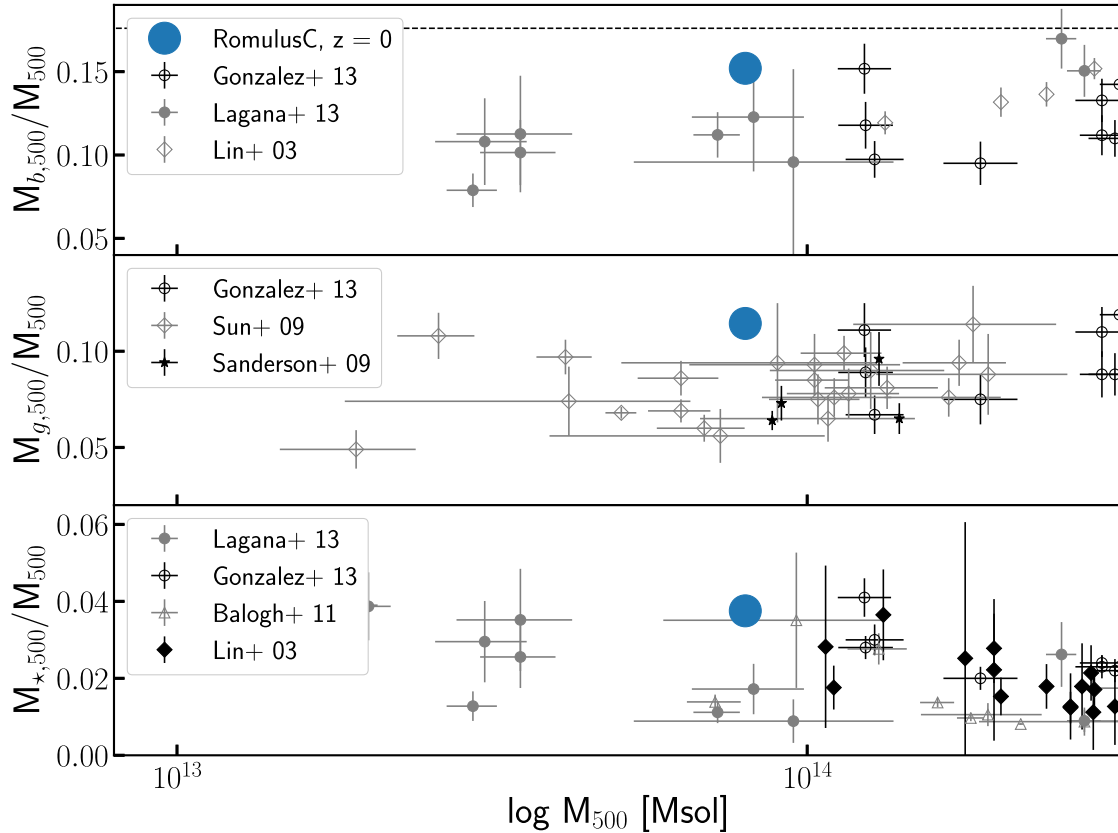


Figure 3. The baryon content of clusters. The total baryon fraction (top), hot gas fraction (middle), and stellar fraction (bottom) by mass in both observed clusters (Lin, Mohr & Stanford 2003; Sanderson, O’Sullivan & Ponman 2009; Sun et al. 2009; Balogh et al. 2011; Gonzalez et al. 2013; Laganá et al. 2013) and ROMULUSC (blue points). All mass fractions for ROMULUSC are within a factor of two of the mean observations at similar masses and within the scatter. We only show $z = 0$ values for ROMULUSC, but confirm that there is negligible evolution in this respect from $z = 0.3$. All observations are for local (redshift below ~ 0.1) clusters, though the Laganá et al. (2013) data extend out to higher redshifts.

sults from ROMULUSC plotted as blue points at both $z = 0.3$ and $z = 0$. Again, the average between mass- and emission-weighted temperature values is used, following Liang et al. (2016). The electron density is calculated as a volume-weighted average within each annulus. At R_{500} , ROMULUSC lies comfortably among the observed low mass clusters. Closer to the centre, the entropy is slightly lower in ROMULUSC compared with the average of observations but it is still within the lower edge of observed clusters. The results are insensitive to the width of the annuli. Once again, we exclude gas with density greater than $500\rho_{\text{crit}}$.

Fig. 6 plots gas temperature, entropy, density, and pressure profiles for ROMULUSC at $z = 0.3$ – 0.5 and compares each to the average profiles observed in cool-core clusters (Arnaud et al. 2010; McDonald et al. 2013, 2014) as well as the average density profile for all clusters (McDonald et al. 2017). While we only include hot ($> 10^6$ K) gas in our analysis, no density criterion is used to generate these profiles. For entropy and pressure we derive P_{500} and S_{500} in the same way as described in McDonald et al. (2014) using T_{500} and the average density. The average density is calculated from the electron density, following McDonald et al. (2014, 2017). For pressure we also normalize by $f(M) = (M_{500}/3 \times 10^{14} h_{70}^{-1} M_{\odot})^{0.12}$ in order to compare effectively with clusters of different mass and assuming the universal pressure profile derived in Nagai, Kravtsov & Vikhlinin (2007).

In the density profile, we see that ROMULUSC matches well with the overall cluster population down to $\sim 0.2R_{500}$, which is where

deviations from self-similarity are seen in observed clusters (McDonald et al. 2013, 2017). Below this scale, ROMULUSC fits well to the median density profile for cool-core clusters from McDonald et al. (2013). The average observed entropy, pressure, and temperature profiles are all calculated from cool-core selected clusters, so ROMULUSC matches them well down to small scales, although the temperature inside $0.2R_{500}$ is biased high. The error bars for these average fits are standard errors from the mean (standard deviation divided by \sqrt{N}) and there is actually a wide range of temperatures from individual observations spanning 0.5 – $2 T_{500}$ within $0.2R_{500}$ (see fig. 13 in McDonald et al. 2014).

We stress that the mass of ROMULUSC is significantly lower than the clusters examined in McDonald et al. (2014, 2017), which may also affect this comparison. Although the pressure profiles are normalized accordingly assuming a universal profile (Nagai et al. 2007), the fact that the data from Arnaud et al. (2010) is for clusters of mass more similar to ROMULUSC might be why we match those results better within $0.2R_{500}$, where self-similarity is no longer valid. We use 3D profiles while the observations are not deprojected, though as shown in McDonald et al. (2014) the deprojected profiles are nearly identical to the projected ones for observed clusters.

Matching the observed structure and baryonic content of the ICM is a particularly important result because, as we will explore further in Section 4.1, by $z = 0.3$ – 0.5 the central AGN has already been (and continues to be) very active in the cluster. The AGN feedback

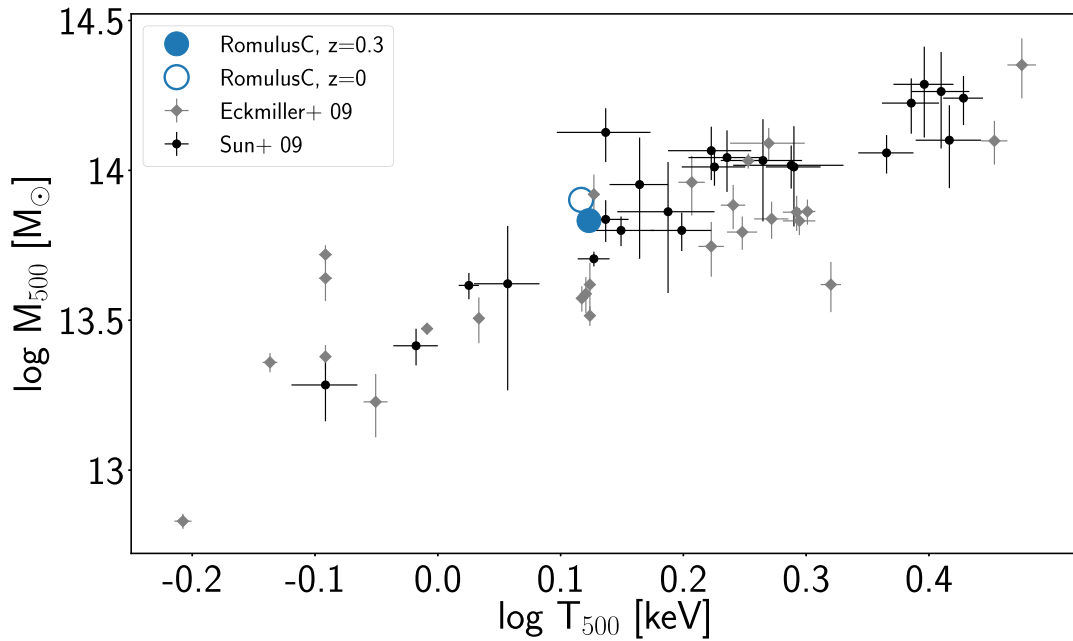


Figure 4. The temperature of the ICM. The observed relationship between group and cluster masses (M_{500}) and the core excised temperature, T_{500} . The open blue circle represents ROMULUSC at $z = 0$ and the solid circle at $z = 0.3$, when the cluster is still in equilibrium prior to the in-fall of a galaxy group and what will be an on-going merger at $z = 0$. To calculate the temperature we use an average between the emission-weighted and mass-weighted results for diffuse ($\rho < 500\rho_{\text{crit}}$), hot gas detectable by X-ray observatories ($T > 0.1$ keV). This decision is based on results from Liang et al. (2016) showing that this average better approximates results from more detailed spectroscopic models at this mass scale and are therefore closer to what an observer would see. Our results are insensitive to this choice.

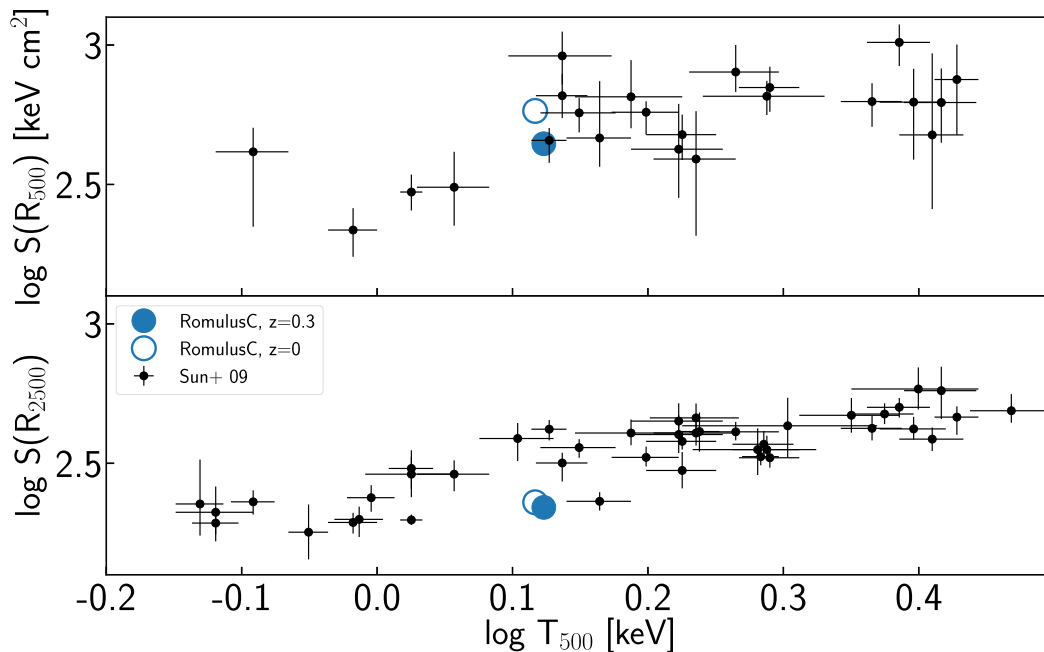


Figure 5. The entropy of the ICM. The observed relationship between entropy and overall cluster temperature. The blue points represent results from ROMULUSC at $z = 0$ (open) and $z = 0.3$ (solid). The entropy is measured within 1 kpc thick annuli at R_{2500} (bottom) and R_{500} (top). Like in Fig. 4, we take the average between mass- and emission-weighted values for temperature to calculate entropy. Again, only diffuse, hot gas is included in the analysis.

in ROMULUSC is able to suppress cooling without disrupting the cool-core structure, similar to the observed clusters that maintain a stable entropy profile over long time-scales (McDonald et al. 2014). In observations and in ROMULUSC, AGN feedback is able to provide

a long-term balance to ICM cooling without disrupting the ICM structure. The effect of feedback is also why we see such strong fluctuations in the temperature and entropy profiles at very small radii.

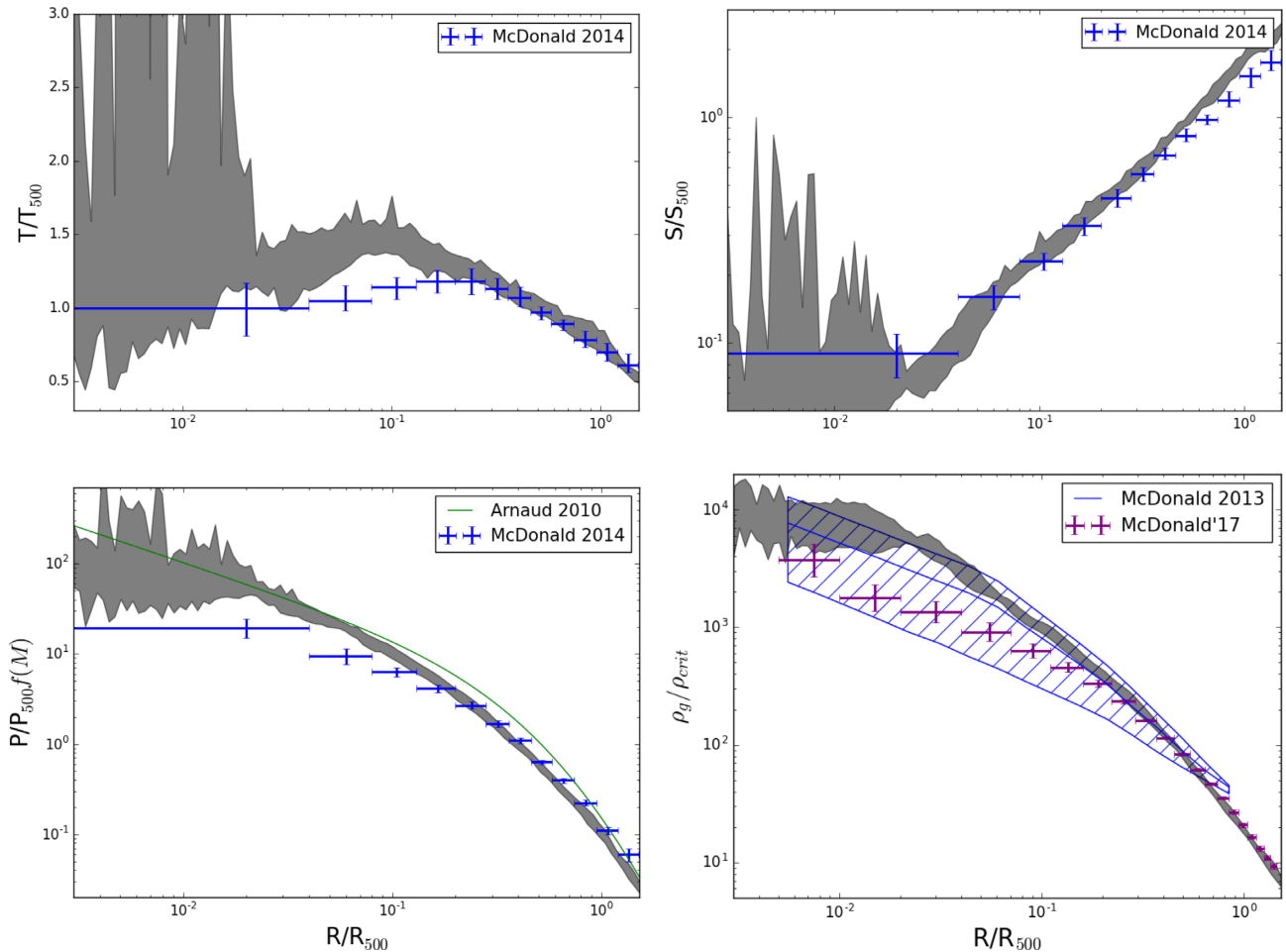


Figure 6. The structure of the ICM. Radial profiles of the temperature, entropy, pressure, and density of the ICM gas in ROMULUSC (grey bands). The grey bands correspond to the range of profiles from $z = 0.3$ – 0.5 . This redshift range was chosen because it corresponds to a period in the simulation prior to the late-time major merger where the cluster still has a cool core. It is also a similar redshift range as the clusters examined in McDonald et al. (2014). At $z < 0.3$ the in-falling group causes increasing disturbance away from equilibrium. As stated in the text, we will examine the effect of this merger on the ICM properties in future work. Overplotted are the results from McDonald et al. (2013, 2014, 2017). For pressure we also compare with results from Arnaud et al. (2010) which are at lower redshifts, but include more similar mass clusters to ROMULUSC. All observed data sets are selected to be cool-core clusters, except for the mean density profile from McDonald et al. (2017). Overall, ROMULUSC fits well with average profiles of cool-core clusters. Compared to McDonald et al. (2014) ROMULUSC has slightly high temperature and pressure within the inner $0.2R_{500}$, but matches well with the Arnaud et al. (2010) results for pressure within $0.2R_{500}$. The density profile matches well with the average profile for all clusters from McDonald et al. (2017), but deviates from self-similarity on small scales where it matches much better median density profile for clusters selected to have low-entropy cores (McDonald et al. 2013).

4 GALAXY EVOLUTION IN CLUSTERS

Now that we have established that ROMULUSC results in a cluster with realistic ICM properties, we turn our focus to the evolution of galaxies within the cluster environment. ROMULUSC represents a relatively rare, dense environment. For reference, the cluster attains $M_{200} = 2 \times 10^{13} M_{\odot}$ by $z = 2$, a mass equivalent to the highest mass halo in the ROMULUS25 25^3 Mpc^3 uniform volume simulation at $z = 0$ (see Fig. 2). ROMULUSC therefore traces galaxy evolution within a very dense environment out to high redshift and, in this sense, represents an important addition to the galaxies followed in ROMULUS25. The fact that ROMULUS25 has the same resolution and sub-grid physics as ROMULUSC means that we can self-consistently compare galaxy properties and evolution between the two simulations in order to examine the effects of a dense environment (ROMULUSC) compared to more isolated galaxies in the field (ROMULUS25). The resolution of the ROMULUS simulations means that we can resolve the evolution of dwarf galaxies in cluster environments better

than ever before. While in the following analysis we focus on the population of galaxies and their bulk properties, in future work we will study the evolution of the internal structures of cluster galaxies over a wide range of stellar masses.

4.1 The brightest cluster galaxy

The most unique cluster galaxy is, of course, the most massive, BCG which, in ROMULUSC, lies in the centre of the halo. This is the first time a galaxy of this size has been simulated at such high resolution in a fully cosmological simulation. Not only will examining this galaxy help us to better understand the interaction between AGN feedback, the central ICM, and the evolution of the BCG, it also represents an important test of our sub-grid physics. As stated in Section 2.3, the sub-grid recipes for star formation, SN feedback, and SMBH physics were calibrated to reproduce observed lower mass galaxies (MW mass and below) and, as demonstrated by

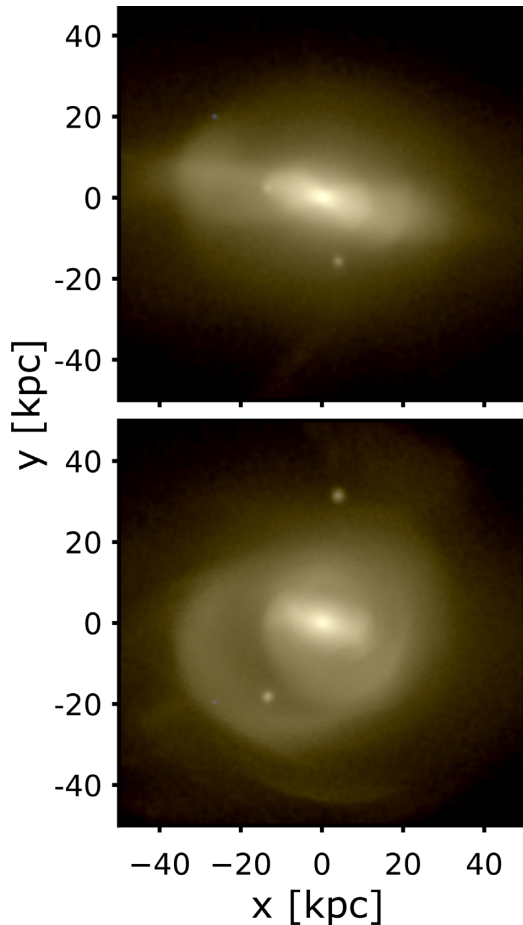


Figure 7. The brightest cluster galaxy. A uvj image of the brightest cluster galaxy in ROMULUSC at $z = 0$ down to $26 \text{ mag arcsec}^{-2}$ to show structure on larger scales. The lack of recent star formation has made the galaxy appear very red. Two orthogonal views are shown. There is no longer any stellar disc structure.

Tremmel et al. (2017), have shown success in reproducing observed properties of galaxies in haloes as massive as $10^{13} M_{\odot}$. The ability of such a model to extend over two orders of magnitude in halo mass and still produce realistic central galaxies is a testimony to the success of our optimization routine. It also means that our results are purely a prediction of our simulation with no tuning for cluster environments.

Fig. 7 shows a synthetic image of the stars in the BCG from two different angles at $z = 0$. The galaxy is being disturbed by an ongoing merger, causing a shell-like structure in the diffuse stars. The morphology is that of a dense stellar core with an extended stellar halo and little recent star formation. The stars associated with the cluster halo not inside of substructure extends out to large radii and are difficult to observe. Recent observations have been able to examine the stellar mass of the central galaxy and its extended stellar halo with unprecedented detail (Gonzalez et al. 2013; DeMaio et al. 2018; Kravtsov et al. 2018). In Fig. 8 we plot the stellar mass within 50 kpc of halo centre in ROMULUSC to compare with recent observations by DeMaio et al. (2018) and Kravtsov et al. (2018) as a function of M_{500} . We also show the results of abundance matching presented in Kravtsov et al. (2018). The stellar mass of the ROMULUSC BCG is slightly high relative to abundance matching results and a factor of ~ 2 higher than the median observed value. While in the simulation we are able to take a 3D stellar

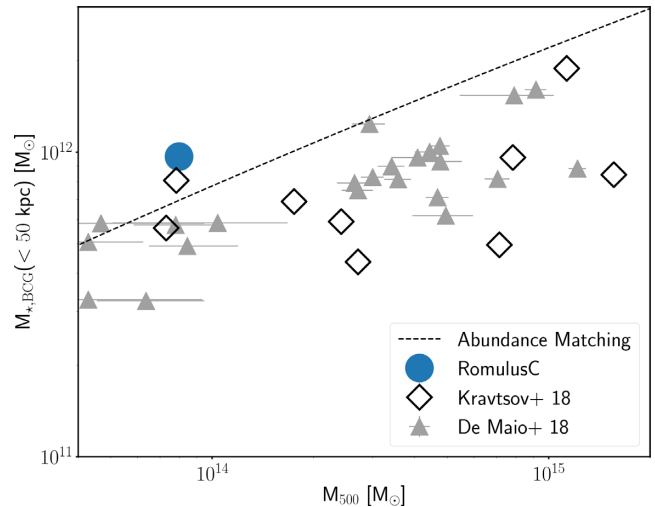


Figure 8. Stellar mass halo mass relation. The relationship between the mass of the central BCG and M_{500} for ROMULUSC (blue point) as well as recent observations from Kravtsov, Vikhlinin & Meshcheryakov (2018) and DeMaio et al. (2018) (black diamonds and grey triangles). Following the observations we compare with here, we consider the stellar mass within 50 kpc from halo centre. Again, we do not plot the $z = 0.3$ values because there is negligible change from $z = 0$. The BCG in ROMULUSC is within a factor of ~ 2 of the median observed BCG stellar mass and matches well with abundance matching results derived from updated luminosity functions (Kravtsov et al. 2018).

mass profile, we confirm that projection effects along different lines of sight make no difference in our results. While these results are similar to BCG masses found in lower resolution cosmological simulations (e.g. Pillepich et al. 2018), recent work presented in Ragone-Figueroa et al. (2018) has resulted in more realistic BCG masses, though higher star formation at low redshift compared to observations.

A slightly high stellar mass for the BCG may imply that the efficiency for SMBH feedback coupling should be increased from our fiducial values. This would allow more energetic feedback for less SMBH growth. Currently, in order to attain highly energetic feedback, the SMBH needs to grow rapidly (given our 2 per cent coupling efficiency and 10 per cent radiative efficiency). Such rapid growth requires a lot of relatively dense gas in the cluster centre, which would also lead to star formation. Additional physical processes seem to be common in higher mass systems, such as relativistic jets and associated radio lobes (Dunn & Fabian 2006). These additional processes associated with radiatively inefficient accretion could effectively increase the coupling efficiency of SMBHs in high mass systems, relative to the value we implement here which is held constant across all black holes in the simulation.

While we only have a sample of one simulated BCG, the fact that the stellar mass is within even a factor of ~ 2 of the median of observed BCGs (and near the upper end of the observed scatter) and eventually ceases any substantial star formation is an important result. While outflows from SMBHs that reach out to large radii are important, ROMULUSC demonstrates that modelling such outflows through mechanical prescriptions, which require additional assumptions and free parameters, is not necessarily required. Our implementation of thermal AGN feedback, which is implemented the same way for all black holes in all haloes, appears adequate to match current observations.

4.1.1 The connection between AGN feedback and BCG quenching

Several previous cosmological simulations have demonstrated the importance of AGN feedback in regulating star formation in massive galaxies (Di Matteo, Springel & Hernquist 2005; Teyssier et al. 2011; Schaye et al. 2015; Sijacki et al. 2015; Beckmann et al. 2017; Pontzen et al. 2017) and the same is true for ROMULUSC. The resolution of ROMULUSC allows us to examine the interaction between the central AGN, the ICM, and the gas content and star formation history of the central BCG with unprecedented detail. Fig. 9 shows the specific SFR (sSFR) within $0.1R_{200}$ and the feedback energy ($\epsilon_f \dot{M} c^2$) imparted by the central SMBH (taken to be the brightest SMBH inside 10 kpc of halo centre at any given time). The SMBH feedback rates are presented in 100 Myr bins to reduce the noise and better show overall trends. The SFR of the BCG is calculated in 10 Myr bins.

The specific star formation history closely follows the change in SMBH activity. This is particularly evident at early times. For every trough in the sSFR there is a peak in SMBH activity and when there is a period of SMBH quiescence there is a rise in sSFR. There are a few instances with particularly powerful ($\dot{E} > 10^{44}$ erg s $^{-1}$) feedback events, but the one occurring at ~ 8 –10 Gyr is the longest. There is a shorter period of energetic AGN activity at 6–7 Gyr, and another phase occurring at 4–6 Gyr that is less continuous. It is only during this final 2 Gyr long episode that large-scale, powerful outflows persist (Fig. 11) and star formation finally plummets in the BCG.

It is common for cool-core clusters to have non-negligible star formation ranging from several to 10s and sometimes up to 100s M_{\odot} yr $^{-1}$ (e.g. Bildfell et al. 2008; Loubser et al. 2016). Consistent with these observations, the BCG in ROMULUSC maintains an SFR around 1–10 M_{\odot} yr $^{-1}$ even after the sSFR drops well below 10^{-11} yr $^{-1}$ and the central galaxy would be considered quenched. This low level star formation continues until the cool core of the cluster is disrupted by an infalling group at $z \sim 0.2$. For the purposes of our analysis here we do not focus on the ICM or BCG evolution during this merger, which is still ongoing at $z = 0$, but analysis of the impact of this event will be the focus of future work. The star formation history of the BCG is remarkably similar to the median sSFR values presented in Bonaventura et al. (2017), which are derived from IR detections of clusters. The McDonald et al. (2016) results use multiple methods to estimate star formation at various wavelengths, but find that cool-core clusters have systematically higher SFRs compared to their overall sample, which could explain why ROMULUSC, which maintains a cool core until $z \sim 0.2$, would also have comparatively more star formation.

It is important to remember that the thermal coupling of AGN feedback is a *local* phenomenon in the simulation. Energy is transferred only to the 32 nearest gas particles (generally within ~ 100 pc of the SMBH). Any outflows that are generated are the natural consequence of hydrodynamic processes occurring as a result of this thermal heating.

Fig. 10 shows the central region of ROMULUSC at $z = 0.53$, just after the sSFR begins to decline and the AGN begins a prolonged period of activity. Different properties of the gas are shown, averaged by mass along a 30 kpc slab (5 kpc for the inset figures), except for the column density plots which are all integrated over 100 kpc, similar to observed radio sources and X-ray cavities that can extend out to 10s to over 100 kpc from the centre of the BCG (e.g. McNamara et al. 2000, 2009; McNamara & Nulsen 2012; O’Sullivan et al. 2012). The large-scale, collimated outflow is clearly seen in the temperature and entropy figures, which both have velocity fields overplotted. The outflowing gas is typically travelling at a few

thousands of km s $^{-1}$ and extends beyond $0.1R_{200}$. Such large-scale outflows dissipate their energy through shocks, as well as turbulent dissipation, and are able to contain cooling within the central regions of the halo. Shocks can be seen in the pressure plot propagating through the innermost core of the halo. Two cavities can be seen in the column density figure. They are associated with the end of the outflow and are reminiscent of X-ray cavities (or radio lobes) expanding due to the injection of hot, high pressure gas from the outflows.

Fig. 11 shows several time-steps between 5 and 11 Gyr. Large-scale outflows from the AGN are commonplace throughout the simulation, but the powerful outflows taking place at $t > 8$ Gyr are able to finally quench star formation. The onset of quenching and these powerful outflows are coincident with a prolonged phase of SMBH activity with feedback rates exceeding 10^{44} erg s $^{-1}$ nearly continuously over 2 Gyr.

The outflows also interact with the ICM on larger scales and change directions due to bulk shear flows. Such mechanisms involving ‘ICM weather’ have been suggested as a way to overcome the problems with fixed-direction jets (e.g. Heinz et al. 2006; Soker & Bisker 2006; Morsony et al. 2010; Mendygral, Jones & Dolag 2012). At the time shown in Fig. 10 ($z = 0.53$) we do find a shear velocity of ~ 100 km s $^{-1}$ between the gas at scales below 50 kpc from the cluster centre and that between 50 and 100 kpc. We also measure a shear of ~ 60 km s $^{-1}$ between 0–30 and 30–60 kpc. These values are relatively small and consistent with other cosmological simulations (Lau et al. 2017) and slightly lower than results from Hitomi’s observations of the Perseus cluster (Hitomi Collaboration 2016). We confirmed that the central BCG is not moving significantly with respect to the centre of mass of the cluster (as measured from a variety of different radial scales). Rather, the shear observed here is likely due to a recent pericentric passage of a cluster galaxy. Shear velocities as low as 100–300 km s $^{-1}$ may be able to have a substantial impact on outflow structure (Hardcastle, Sakelliou & Worrall 2005). Of course, the structure of the outflow is developed over a long period of time while here we only examine a single snapshot. A deeper analysis is needed to better understand this large-scale evolution of the wind structure, which will be conducted in future work.

4.1.2 The effect of AGN feedback on the ICM

AGN feedback does not limit star formation by evacuating nor directly heating gas in the inner cluster core. Fig. 12 plots the mass of gas within $0.1R_{200}$ as a function of time. The overall supply of gas rises at early times while the cluster progenitor is still growing rapidly (see Fig. 2), then remains nearly constant from ~ 4 Gyr onwards. However, following the series of very powerful feedback events at $t > 8$ Gyr, the cold gas (or, equivalently, the HI gas, which is tracked self-consistently in the simulation) supply declines along with the sSFR. During this time when quenching is in progress or completed (8–11.7 Gyr), the AGN is not drastically increasing the entropy or cooling time of the gas. Fig. 13 shows the time evolution of the mass-weighted entropy and cooling time profiles for ROMULUSC. Within the central $\sim 0.05R_{200}$, both entropy and cooling times are low and indicative of a cool-core/relaxed ICM. The time during which the central BCG is becoming quenched is marked between two vertical dashed lines. The cluster core is able to survive with low entropy and cooling time-scales of $\sim 10^8$ yr throughout the period where star formation is quenching. This is consistent with observed findings that cool-core clusters are more likely to host radio-loud AGN (e.g. Mittal et al. 2009). It is also

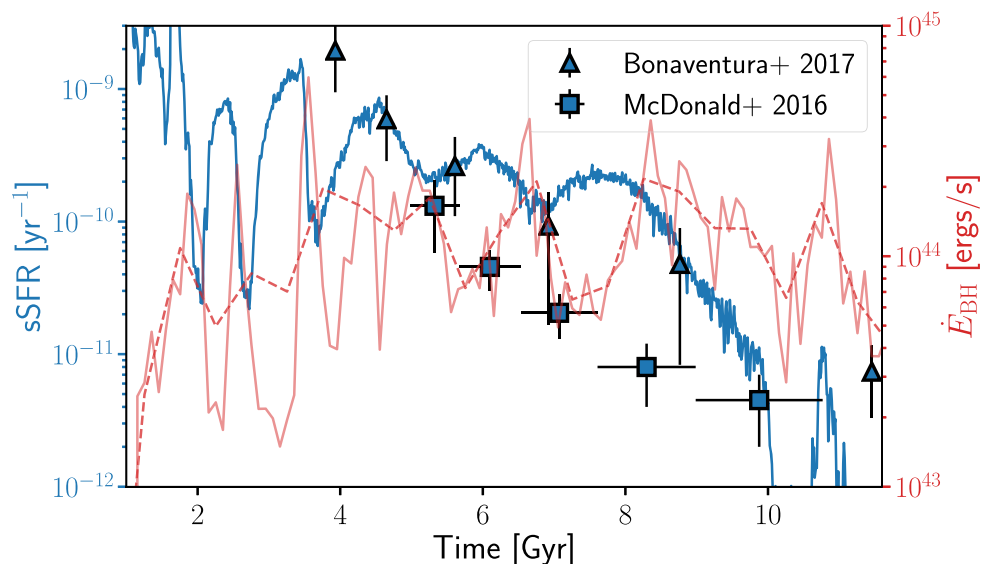


Figure 9. Star formation and SMBH feedback history. The specific star formation rate (blue, averaged over 10 Myr bins) and feedback rate of the central SMBH (red, averaged over 100 and 500 Myr bins for solid and dashed lines, respectively) for the BCG in ROMULUSC. The SMBH feedback traces both accretion and feedback energy imparted by the SMBH on to nearby gas. Dips in the sSFR are often associated with peaks of SMBH activity. The peak of activity beginning around 8 Gyr and persisting through 10 Gyr is associated with the final quenching of the BCG. The sSFR history of the ROMULUSC BCG is remarkably close to the average evolution observed in clusters from Bonaventura et al. (2017), but slightly high compared to results from McDonald et al. (2016). The range in time shown is cut off just prior to the infall of the group seen in Fig. 7. The merger destroys the cool core, a topic to be explored in future work.

in agreement with high-resolution simulations of isolated galaxies, which show how AGN-driven outflows have little direct effect on the gas within their host galaxy (Gabor & Bournaud 2014).

The vertical solid line indicates the time where a major merger with a nearby group causes the cool core to be destroyed, an event that is apparent in the nearly flat entropy and cooling time profiles after this time. As stated previously, we will examine this merger event and cool-core destruction in future work, but use it here as an illustrative comparison between the effect of a major merger and that of AGN feedback.

4.2 Cluster member galaxies

An important advantage of ROMULUSC’s resolution is the ability to better resolve cluster galaxies down to smaller masses than ever before. Our threshold for what is ‘resolved’ in ROMULUSC is very conservative. In the following analysis we only consider haloes of total mass at least $3 \times 10^9 M_{\odot}$, corresponding to a minimum dark matter particle count of $\sim 10^4$ per halo. We compare galaxy evolution in the cluster and protocluster environments simulated in ROMULUSC to galaxy evolution in isolated field galaxies simulated in ROMULUS25.

The zoom-in Lagrangian region used to model ROMULUSC extends, at $z = 0$, approximately out to $2R_{200}$. We only include galaxies in our analysis that are ‘uncontaminated’ with low-resolution dark matter particles, thereby selecting only those galaxies that lie well within the high-resolution region. We still caution that galaxies near the boundaries may still have been affected by the lower resolution regions nearby, but even when we include all uncontaminated galaxies in the zoom region such affected galaxies would be rare. While we do discuss projection effects in the following sections, all results are presented using 3D radial bins relative to the cluster centre. Having only a single system makes ROMULUSC more susceptible to spurious results due to the exact choice of projection.

Further, because of the limited zoom-in region size, we would still not be able to approximate the full effects of contamination from non-cluster galaxies at large radii.

In order to compare with galaxy evolution in relatively low-density environments, we extract central, relatively isolated galaxies from ROMULUS25 based on the criteria that they do not exist within R_{200} of any halo hosting a central galaxy of similar or greater stellar mass. For galaxies in ROMULUS25 with stellar masses below $10^{10} M_{\odot}$, we apply an additional criteria that they be no closer than 1.5 Mpc from any galaxy with stellar mass greater than $2.5 \times 10^{10} M_{\odot}$ to be considered isolated field galaxies. This is motivated by results from Geha et al. (2012) that show environmental quenching in low-mass galaxies taking place at such scales. Following the results of Munshi et al. (2013) that account for limitations in observing the total stellar mass of a galaxy, we define the observed stellar mass of a halo’s central galaxy to be $0.6M_{*,\text{tot}}$, where $M_{*,\text{tot}}$ is the total stellar mass of the halo. We confirm that at the halo masses we examine here, and given our criteria for isolated galaxies, our results would not change were we to explicitly remove satellite galaxy contributions, which do not account for a significant portion of the total stellar mass.

4.2.1 Environmental quenching

In order to obtain a self-consistent picture of quenching in both ROMULUSC and ROMULUS25, we define a star forming main sequence based on central, isolated galaxies in ROMULUS25. We follow a similar procedure to observations (e.g. Bluck et al. 2016) and fit the median values of the SFR within 0.1 dex bins of stellar mass between 10^8 and $10^{10} M_{\odot}$. We find a best-fitting main sequence of $\log(\text{SFR}) = 1.206 \times \log(M_*) - 11.7$ for $z = 0$. While this differs from main sequence definitions derived from observations in both slope and normalization, for stellar masses between 10^8 and $10^{10} M_{\odot}$ the fit lies within the 0.5 dex scatter associated with the

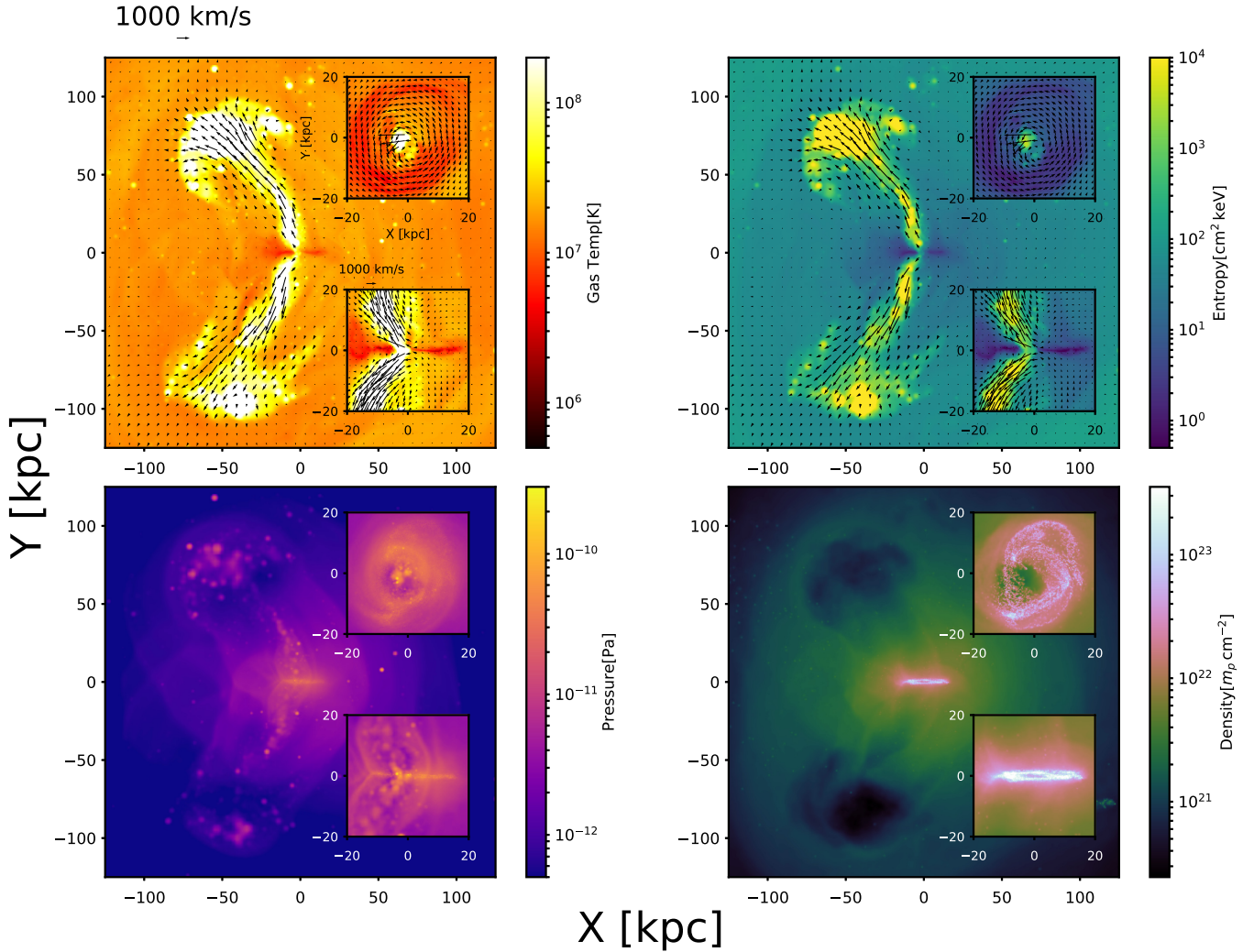


Figure 10. Outflows in action. Images of temperature (top left), entropy (top right), pressure (bottom left), and column density (bottom right) of cluster gas at $z = 0.53$ ($t = 8.41$). Each large panel is a mass-weighted slice along a 30 kpc slice through the centre of the cluster. The inset panels are 5 kpc slices zooming into the central regions. The exception to this is the density plot, which is a 100 kpc slice for all panels in order to better show the structure of the gas. A large-scale outflow is clearly seen in the temperature and entropy plots, which also overlay the velocity field. The gas in the outflow is moving at 1000 km s^{-1} . The structure of the outflow is less clear in the pressure plot; the outflow has a similar pressure as the ambient gas, which is how it is able to maintain its collimation. The tips of the outflow show a high-pressure, low-density region, which can be seen to create bubbles in the gas, similar to what is observed in X-ray cavities. Although the outflow is powerful, it coexists with low entropy, 10^6 K , rotationally supported core. Shocks can be seen propagating through the inner regions in the pressure plot, helping to balance the cooling as seen in, e.g. Li et al. (2015).

observed main sequence. We take any galaxy whose star formation is a factor of 10 below our fitted main sequence to be quenched at $z = 0$. To calculate star formation, we use the formation times of star particles within each halo and calculate the average formation rate in the previous 25 Myr. However, because of limited mass resolution, the smallest possible SFRs are quantized and therefore subject to numerical noise. For haloes that formed only two or fewer particles in the previous 25 Myr (corresponding to an SFR of $0.064 M_{\odot} \text{ yr}^{-1}$), we calculate the SFR averaged over the previous 250 Myr instead. We confirm that our results are insensitive to the choice of time-scale over which to measure SFR except for the lowest mass galaxies.

This definition of ‘quenched’ does differ from some observations, including Wetzel et al. (2012), who adopt a flat threshold of 10^{-11} yr^{-1} . Based on our main sequence definition, quenched galaxies are defined on a mass-dependent specific SFR threshold

between 10^{-11} and $10^{-10.5} \text{ yr}^{-1}$ at $z = 0$ across the stellar mass range we cover. Wetzel et al. (2012) find what would be considered a nearly constant main sequence in specific SFR, while our main sequence has a slight evolution with mass. As discussed briefly in Bluck et al. (2016), because the simulations are not equipped to fully mimic the SFR diagnostics that observers use, such a definition allows us to define a quenched threshold that is fully self-consistent for our simulated galaxies while still maintaining the ability to compare with observations that have a different distribution of (inferred) SFRs. Our definition is also not reliant on the factor of ~ 2 difference between the total stellar masses of our simulated galaxies and those that would be inferred by observations (Munshi et al. 2013), which would add further uncertainty to our results. Finally, this threshold definition allows us to derive self-consistent quenched fractions at different redshifts. We confirm that changing our threshold to a flat sSFR value of 10^{-11} yr^{-1} will affect the $z = 0$ classification of a

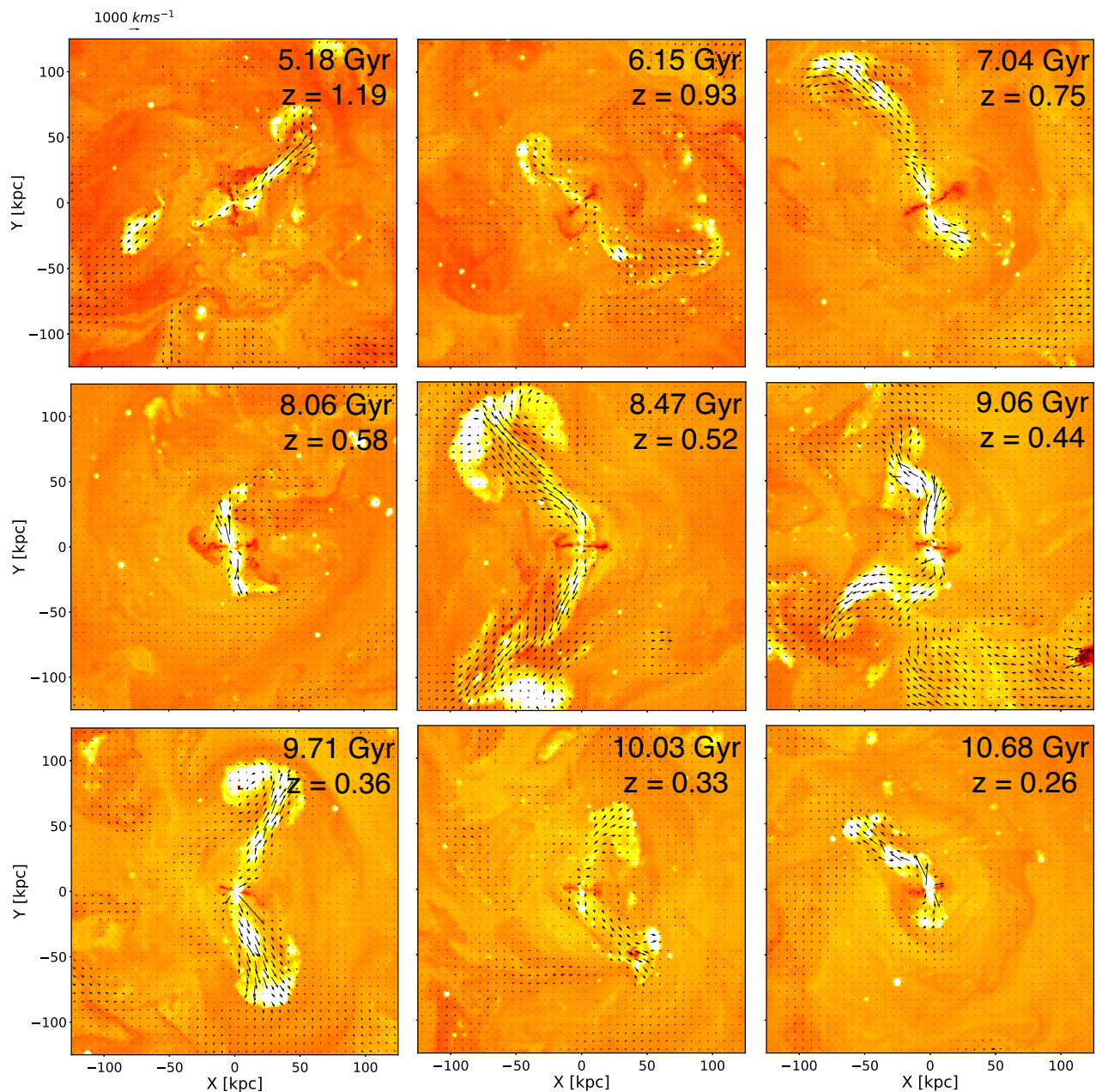


Figure 11. AGN-driven outflows over time. Snapshots of the gas temperature and velocity field in the inner regions of ROMULUSC over cosmic time. Each image shows the same projection, modulo rotations about the y -axis in order to best image capture any outflow structures present. The colours are the same as Fig. 10. The temperatures are mass-weighted averages along a 2 kpc slice centred at halo centre. It is clear that the winds evolve in direction, shape, and magnitude. The direction is dictated by the rotation of gas in the inner 10–20 kpc of the halo as well as the larger scale motions of the ICM. Between 8 and 10 Gyr, the outflows are particularly strong, corresponding to a period of both high SMBH activity and declining star formation in the BCG (see Fig. 9).

handful of the most massive galaxies in both ROMULUS25 and ROMULUSC, bringing the quenched fraction lower for the highest mass bin in both simulations but still within the 68 per cent confidence interval for our fiducial definition (see Fig. 14). We also confirm that our definition of quenched is consistent with a definition based on UVJ colours (e.g. Whitaker et al. 2011).

Fig. 14 plots the quenched fraction of galaxies as a function of mass for both ROMULUS25 (blue) and ROMULUSC (orange). In both simulations there are >20 galaxies per bin (>100 for the lowest masses) except for the highest mass bins that contain 7

and 12 galaxies for ROMULUSC and ROMULUS25, respectively. For ROMULUSC galaxies, here we only consider those within R_{200} of the cluster centre in order to compare directly with observations from Wetzel et al. (2012). The quenched fractions from ROMULUS25 are mostly consistent with results from SDSS (Bluck et al. 2016) at higher masses, following the same increasing trend with stellar mass, although the quenched fractions from ROMULUS25 are biased low, particularly in the highest mass bin. However, the fact that our predictions are roughly consistent with observations and follow the same trend in gradually increasing with mass is encouraging. More

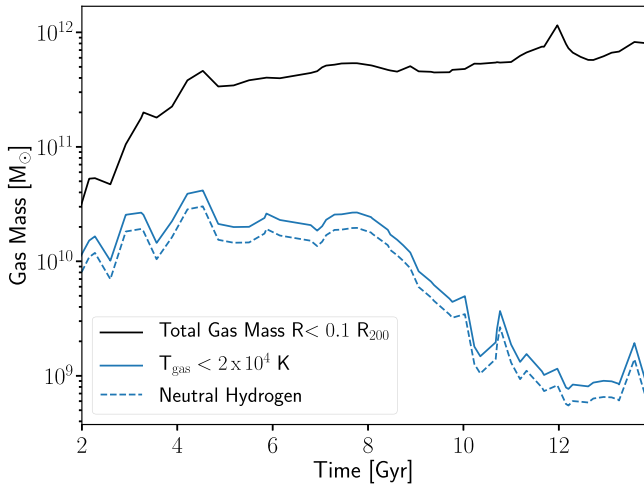


Figure 12. Central gas content of the BCG. The total (black line), cold (blue solid), and HI (blue dashed) gas masses within the central $0.1 R_{200}$ for ROMULUSC. Large-scale feedback from the central SMBH taking place after 8 Gyr results in depletion of cold gas in the central regions without affecting the overall gas supply.

work is needed to explain this discrepancy which is beyond the scope of this paper.

At the low mass end, ROMULUS25 predicts very low quenched fractions, similar to observations. However, at the lowest masses our fractions of several per cent are still significantly higher than observations from Geha et al. (2012). Exploring this difference in more detail is beyond the scope of this paper, but can be due to several factors. Our definition of quenched is based on direct SFRs from the simulation, as opposed to Geha et al. (2012), where quenching is defined on the basis of $H\alpha$ emission as well as old stellar ages derived from D_{4000} . It is possible that low level and/or recent star formation in these small galaxies would make them non-quenched in the Geha et al. (2012) definition. There is also evidence that a subset of low-mass galaxies have low gas fractions and emission consistent with AGN (Bradford et al. 2018), which could provide enough $H\alpha$ to make a galaxy appear star forming. In future work we plan on doing a more in-depth analysis of the dwarf galaxy population in ROMULUS25 and comparing it in a more self-consistent way to observations. For the purposes of this work, the important point is that we predict very low quenched fractions for low-mass galaxies in isolation.

For ROMULUSC, the highest mass bins are overall comparable to the results from Wetzel et al. (2012), but we do not see the same trend with stellar mass. Of course, given our relatively low number statistics at the higher masses, such a trend would be difficult to resolve. Here we have also tailored our bins to match those used in Wetzel et al. (2012) at masses greater than $10^{9.7} M_{\odot}$, but we combine the final two in order to have enough galaxies in the bin. We do predict significantly higher quenched fractions at $M_{*} = 10^{9.7-10.1} M_{\odot}$. We see a significant difference in the quenched fraction at high masses between cluster and field environments, unlike observations (Wetzel et al. 2012; Bluck et al. 2016). This is likely due to the fact that ROMULUS25 underproduces quenched galaxies at higher masses, making the environmental effects of the cluster more apparent.

For low-mass galaxies, ROMULUSC predicts a nearly constant quenched fraction as stellar masses get smaller. The trend with stellar mass observed at high masses by Wetzel et al. (2012) there-

fore does not continue to lower mass galaxies, with 80–100 per cent of galaxies below $10^{10} M_{\odot}$ predicted to be quenched within R_{200} independent of their stellar mass. This is in stark contrast to galaxies in the field from both observations and ROMULUS25. While the ability to observe such low-mass galaxies is limited, there have been detailed observations within a small number of nearby clusters that show a significant population of quenched dwarf galaxies (e.g. Drinkwater et al. 2001; Weinmann et al. 2011; Balogh et al. 2016; Roediger et al. 2017; Habas et al. 2018). Weinmann et al. (2011) find varying results as to how quenched fractions change with galaxy mass. For Virgo and Coma they find little dependence on luminosity, but clear dependence in Perseus. In all three cases, the quenched fractions presented in Weinmann et al. (2011) range from ~ 70 –90 per cent for dwarf galaxies. The quenched fractions in ROMULUSC are on the high end of these observed clusters, though not inconsistent. These results are also consistent with Geha et al. (2012), who find that the quenched population of low-mass galaxies quickly increases with proximity to higher mass galaxies, even outside of R_{200} . Finally, we also note that these results are consistent with lower resolution cluster simulations (e.g. Bahé et al. 2017) that will be discussed further in Section 5.2.

Fig. 15 plots the fraction of quenched galaxies as a function of radial distance from the cluster centre at $z = 0$ for two stellar mass bins. The high-mass bin was chosen to match that probed by Wetzel et al. (2012) and we find that our results are biased high in comparison. According to Fig. 14, this is due to the $10^{9.7-10.1} M_{\odot}$ galaxies being more quenched in ROMULUSC than in the Wetzel et al. (2012) observations. For these higher mass galaxies we choose the radial bins such that each bin contains 10 galaxies. We confirm that, were we to only include galaxies with $M_{*} > 10^{10} M_{\odot}$, our values would be much more similar to the Wetzel et al. (2012) results. Again we note that projection effects can affect the results from observations such that these points should be considered lower limits, particularly at large separations where contamination from the field can be important. Indeed, we find that the quenched fractions in several radial bins decreases for ROMULUSC if we were to use the projected distances, though the exact effect depends on the line of sight.

While at high masses the radial dependence is difficult to estimate based on the large error bars, we do see some evidence for a decreasing quenched fraction with radius, though possibly not as steep as that presented in Wetzel et al. (2012). For the low-mass bin, we find with more confidence that there is no radial dependence, and the quenched fraction remains steady at ~ 80 –100 per cent out beyond R_{200} . There is some evidence that the quenched fraction does fall off beyond $\sim 1.5 R_{200}$, but we would need a larger sample of galaxies and a larger zoom-in region in order to know for sure.

Our results indicate that the processes causing galaxy quenching in high-density environments are much more efficient compared to the field for all but possibly the highest mass galaxies. For low-mass galaxies, this process is particularly efficient and seems to act evenly at all distance scales. It has been suggested that the main process leading to galaxy quenching in cluster environments is ram pressure stripping and has been supported by observations (e.g. Smith et al. 2010; Merluzzi et al. 2013; Boselli et al. 2014; Roediger et al. 2015; Haines et al. 2013, 2015) as well as both hydrodynamic simulations and analytic models (e.g. Murakami & Babul 1999; Hester 2006; Bahé & McCarthy 2015; Mistani et al. 2016; Zinger et al. 2018). This would explain why observations of higher mass cluster member galaxies have a quenched fraction that negatively correlates with distance, but we predict such radial dependence does not exist for lower mass galaxies. Ram pressure is more efficient at stripping a small galaxy. For a higher mass galaxy

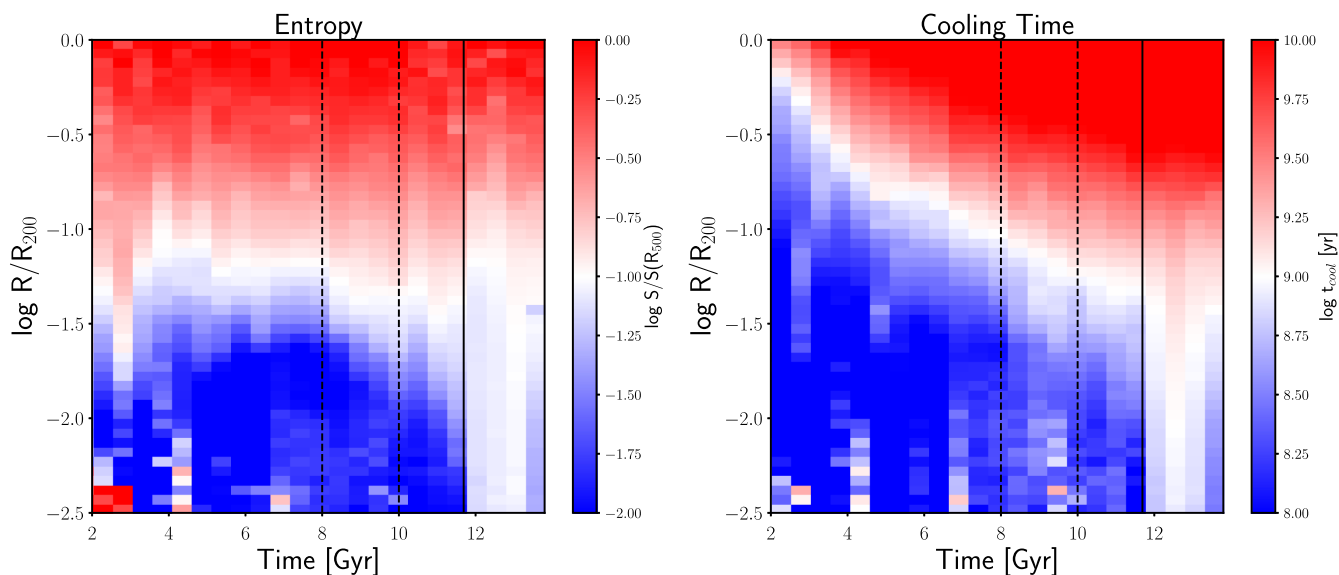


Figure 13. Survival of the cool core. Entropy and cooling time profiles as a function of time for ROMULUSC. Up until the onset of a major merger, marked by the vertical black line, the entropy profile remains steeply declining towards the centre of the halo and the cooling times remain below 1 Gyr, both important characteristics of a cool-core cluster. Between 8 and 10 Gyr, the star formation and amount of cold gas in the central regions declines due to the large-scale AGN feedback, but the cluster maintains a low-entropy core with sub-Gyr cooling times. Following the major merger, the entropy profile flattens out and the cooling times become several Gyr, consistent with non-cool-core systems.

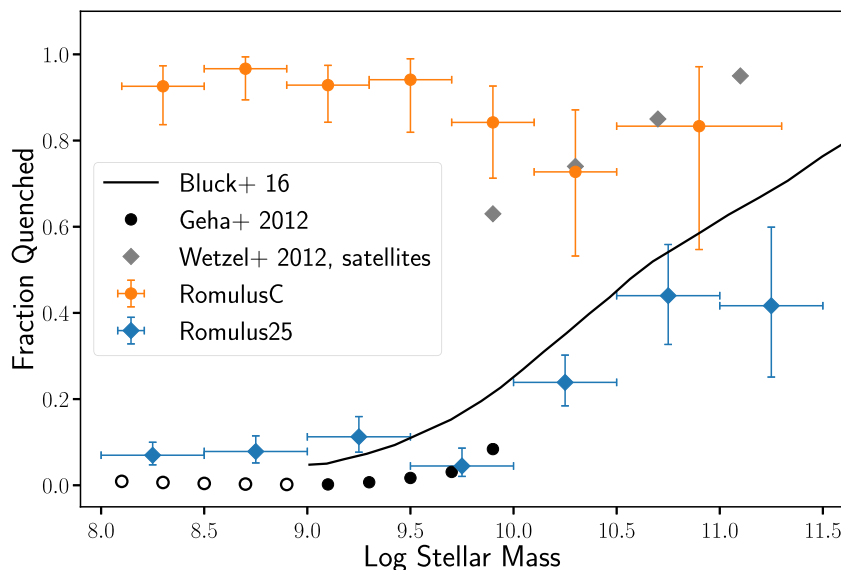


Figure 14. Quenching as a function of stellar mass. The fraction of quenched galaxies as a function of stellar mass for both ROMULUSC (orange points) and ROMULUS25 (blue diamonds). At all but the highest masses we find that satellite galaxies in ROMULUSC have a much higher quenched fraction than isolated galaxies. Our results are consistent with the quenched fraction found by Wetzel et al. (2012), but due to small number statistics we cannot confirm that we also see a trend at high mass. At low masses we find the quenched fraction remains nearly constant at 80–90 per cent. Error bars represent the 68 per cent binomial confidence interval (Cameron 2011). The open points are also from Geha et al. (2012) and represent upper limits.

with a larger gas disc, such processes would take longer and require higher ram pressure, thus becoming more efficient for orbits passing closer to halo centre.

In order to examine the process of quenching in more detail, we follow the evolution of each galaxy that is quenched at $z = 0$ in ROMULUSC within $2R_{200}$, the extent of our high-resolution region at $z = 0$. Fig. 16 plots cumulative distribution functions for various properties of quenched galaxies in ROMULUSC: their final distance from the cluster centre, the distance at which they become quenched,

their minimum distance prior to quenching, and the redshift at which they become quenched. In order to determine when a galaxy is quenched, we compare to the main sequence fitted to ROMULUS25 data as described above. To account for an evolving main sequence, we perform fits at $z = 1, 2,$ and 3 in addition to our $z = 0$ fit and compare galaxies to the main sequence by interpolating between each main sequence. To see whether quenching occurs differently at different masses, we split our sample into high- and low-mass bins around $M_{\star} = 10^{9.7} M_{\odot}$. We choose this splitting because it

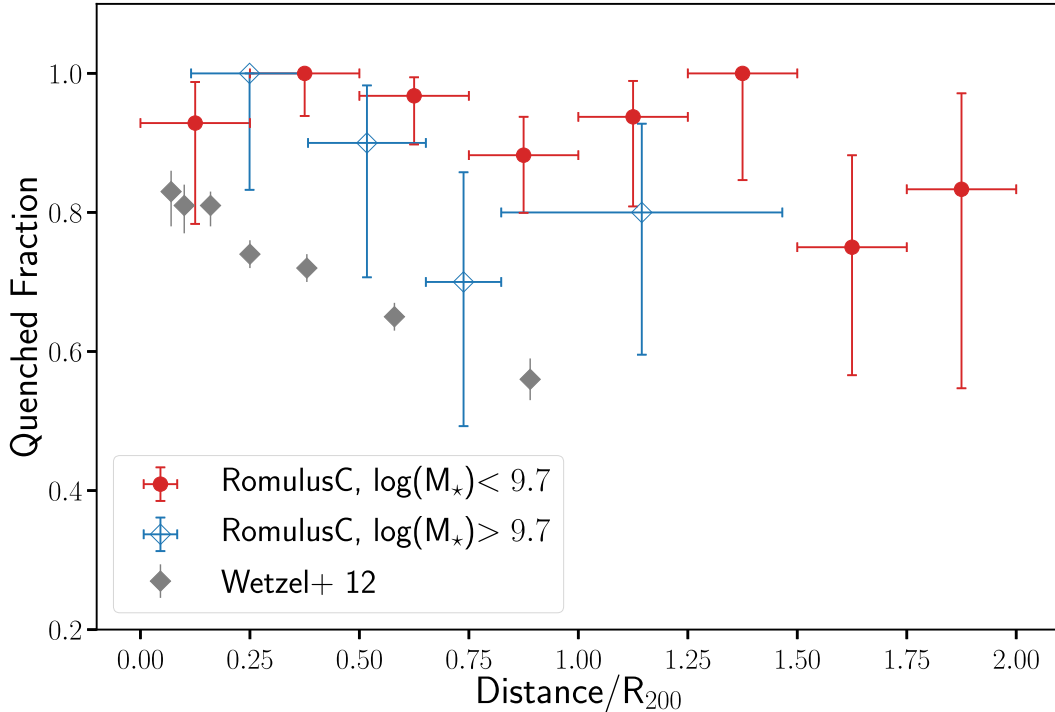


Figure 15. Quenching as a function of position in a cluster. The quenched fraction as a function of distance from halo centre for two mass bins. At high mass (blue, open points; chosen to match the masses of observed cluster galaxies from Wetz et al. 2012) our values are high compared with observations, but as explained in the text this is due to the lowest mass galaxies in this bin. At low masses we predict that no trend exists. At all radial distances low-mass galaxies have a quenched fraction of 80–90 per cent. Error bars represent the 68 per cent binomial confidence interval (Cameron 2011).

corresponds to the lower mass limit of the Wetz et al. (2012) study and represents a rough boundary below which observations of galaxies in cluster environments is limited to a handful of nearby systems. Note that our time resolution for tracking galaxy evolution is limited to ~ 100 Myr, the time between saved snapshots.

We see little difference between high-mass and lower mass galaxies in terms of their quenching redshift, their $z = 0$ final distance to the cluster centre, and the distance at which they become quenched. We do, however, see a significant difference in the minimum distance relative to the cluster centre achieved prior to quenching. Massive, quenched galaxies are more likely to have orbits that take them closer to halo centre before they quench. This supports the idea of ram pressure stripping being the dominant process acting on in-falling cluster galaxies, at least at higher masses. At lower masses multiple processes affect the galaxies’ gas supply. First, 36 per cent of lower mass galaxies have been satellites of haloes prior to cluster in-fall. These galaxies therefore experienced a phase of ‘pre-processing’ by hot halo gas in another halo. At lower masses, galaxies are also more susceptible to ram pressure stripping because of their shallower potential and often explosive stellar feedback processes (Murakami & Babul 1999; Bahé & McCarthy 2015). This difference may also be due to massive galaxies/haloes sinking faster due to dynamical friction, potentially combined with ram pressure taking longer to strip more massive discs. We will examine the role of ram pressure stripping as a driving force of galaxy quenching in more detail in future work.

Importantly, Fig. 16 also shows how the dependence of quenching processes on the position within a cluster can be quickly erased simply by orbital dynamics. The upper left-hand panel implies that quenching in high-mass galaxies on average requires closer approaches to the cluster centre compared with lower mass galaxies.

However, by the time the galaxies quench, this difference is no longer apparent. This is expected if these galaxies are on more eccentric orbits when they quench, as would be the case if they were to quench soon after their initial in-fall before they have virialized, in agreement with results from the Magneticum simulations (Lotz et al. 2018). These radially plunging orbits would take the galaxies near the cluster centre, where they experience a large amount of ram pressure, and then quickly take them back out towards the cluster outskirts. If this first passage is enough to quench star formation, and if the orbit is radial enough, then the galaxy can quickly be taken very far from the cluster centre by the time it quenches. As time goes on, the orbits evolve, particularly as in-falling galaxies virialize and feel the effects of dynamical friction.

4.2.2 The evolution of star formation in cluster galaxies

We follow the evolving population of galaxies within $2R_{200}$ of the cluster’s main progenitor halo in ROMULUSC in order to examine how the population changes over time relative to field galaxies. Fig. 17 shows the quenched fraction of this population of galaxies in ROMULUSC (orange) as a function of their stellar mass at $z = 0, 0.5, 1.0,$ and 2.0 . At each redshift we compare to the population of central, non-interacting galaxies from ROMULUS25 (blue). We find that the enhanced quenched fraction for low-mass galaxies is well established at high redshift. Note that Fig. 16 does not indicate that any $z = 0$ cluster galaxy quenches prior to $z = 2$. This is because all of the galaxies that are quenched at higher redshifts have since merged with another galaxy, most commonly the BCG, or have been otherwise disrupted or stripped so as to no longer be considered resolved substructure in the simulation (based on our very conservative definition of what is adequately resolved).

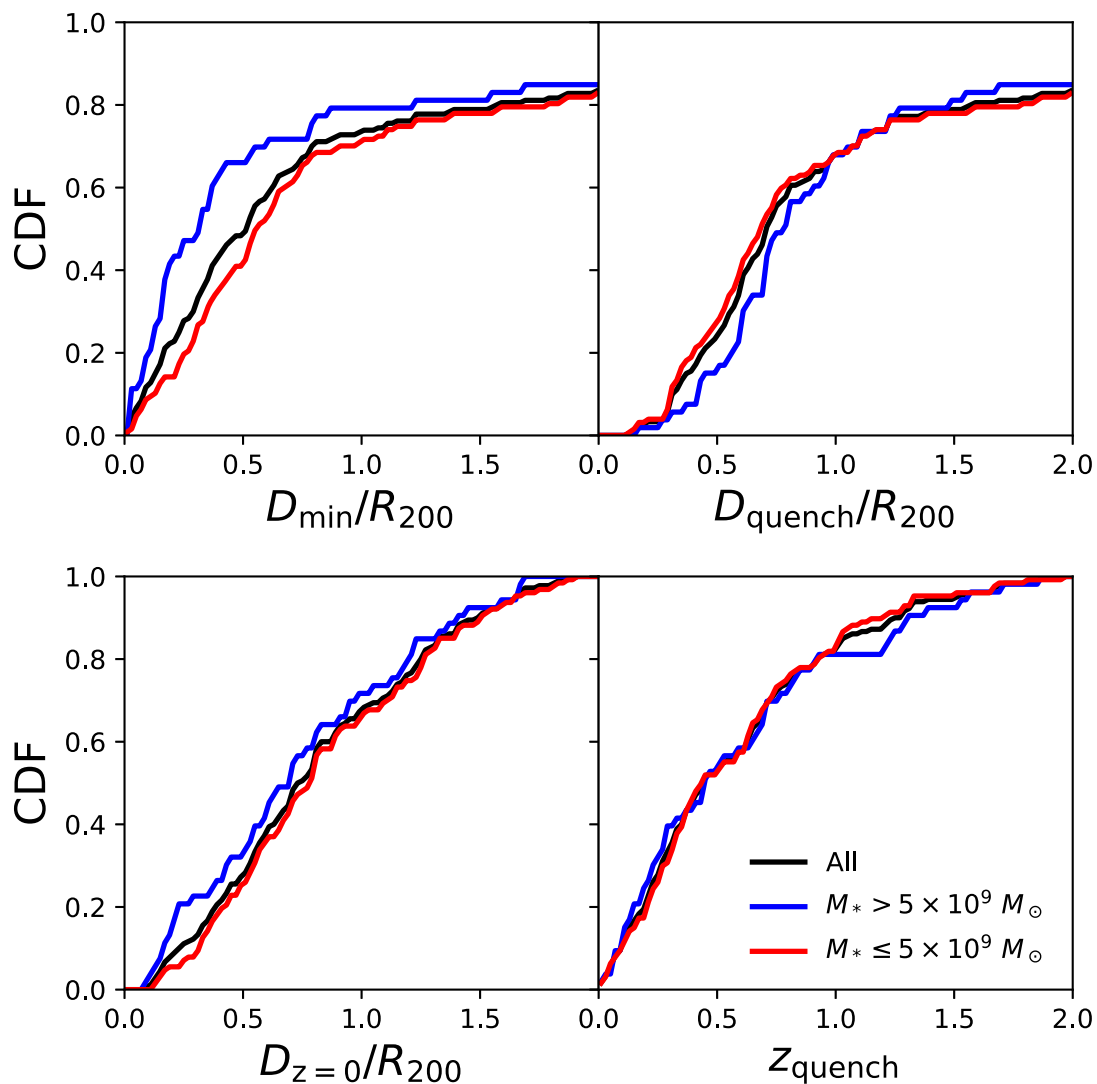


Figure 16. When and where cluster satellites quench. Cumulative distribution functions for quenched massive (blue) and low-mass (red) cluster galaxies. Upper right-hand side: The distribution of minimum distances relative to the cluster centre prior to quenching. Upper left-hand side: The distance at which the galaxies quench (fall below 1 dex relative to the main sequence). Lower left-hand side: The distance of the galaxies at $z = 0$. Lower right-hand side: The redshift when the galaxies quench. There is little distinction between high- and low-mass quenched galaxies in all cases, but for the minimum distance to the cluster centre achieved prior to quenching. High mass quenched galaxies are more likely to have had orbits that took them closer to the cluster centre. This distinction, however, is mostly lost by $z = 0$.

4.2.3 Black hole growth in cluster galaxies

ROMULUSC is the first cosmological cluster simulation to include all three of the following: (1) realistic SMBH dynamics (Tremmel et al. 2015, 2018), (2) SMBH accretion that accounts for the kinematics of gas within the galaxy (Tremmel et al. 2017), and (3) SMBH formation criteria that requires no *a priori* assumptions about halo occupation of SMBHs, seeding them in small haloes (10^8 – $10^{10} M_{\odot}$) at early times (Tremmel et al. 2017). All of this, combined with the high resolution of ROMULUSC means that we can accurately follow SMBH evolution within cluster member galaxies, whose gas, as well as overall morphology, is undergoing tremendous evolution through interactions with both the ICM and other galaxies. Our model allows SMBHs to exist and dynamically evolve within low-mass and high-mass galaxies alike. They are also seeded within those galaxies early enough such that they experience the full effects of the dense cluster environment along with their host galaxy.

Taking galaxies once again within $2R_{200}$ at different redshifts, we examine their SMBH activity compared with the field. Fig. 18 shows the 25th (dotted), 50th (dashed), and 75th (solid) percentiles in average SMBH Eddington ratio over the previous 100 Myr for the SMBH with the highest accretion rate in each galaxy as a function of galaxy mass. The average Eddington ratio is calculated by solving the following equation for f_{Edd} .

$$M_0 + \Delta M = M_0 \exp \left[\frac{f_{\text{Edd}} \cdot (1 - \epsilon)}{\epsilon} \left(\frac{100 \text{ Myr}}{t_{\text{Edd}}} \right) \right], \quad (5)$$

where M_0 is the initial mass of the SMBH at $t_0 = t(z) - 100$ Myr ($t(z)$ is the time at any given redshift) and ΔM is the amount of growth that took place during the previous 100 Myr. The characteristic time-scale for Eddington limited accretion, t_{Edd} , is given by the following equation given a Thomson scattering cross-section, σ_T ,

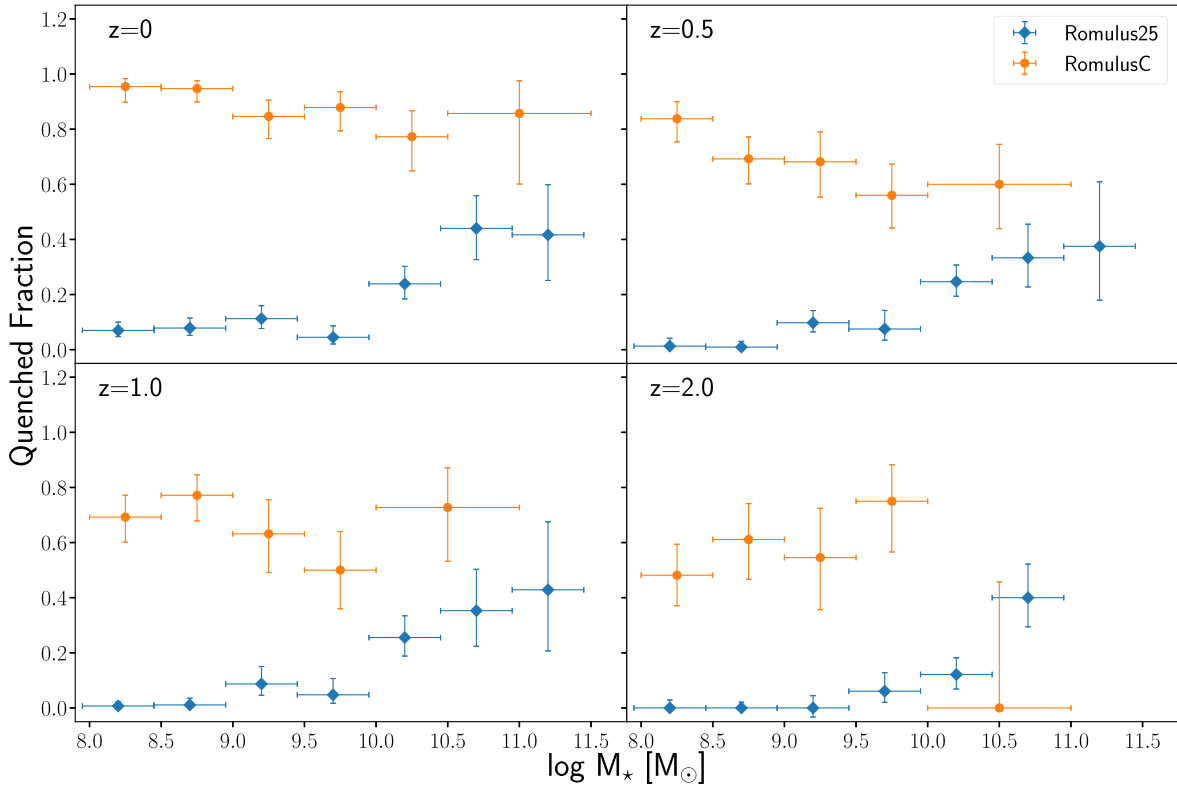


Figure 17. Quenching over cosmic time. The fraction of quenched galaxies as a function of stellar mass in ROMULUSC (orange) and ROMULUS25 (blue) at four different redshifts. All galaxies within $2R_{200}$ are shown. The enhanced quenching seen in high-density environments like ROMULUSC is in place even at high redshift and for low-mass galaxies. Error bars represent the 68 per cent binomial confidence interval (Cameron 2011).

and the mass of a hydrogen atom, m_h .

$$t_{\text{Edd}} = \frac{\sigma_T c}{4\pi G m_h}. \quad (6)$$

Using this relation allows us to account for the fact that the Eddington accretion rate is evolving continuously as the SMBH mass grows. This relation for exponential mass growth is equivalent to what is actually used to calculate mass growth during each SMBH time-step, Δt , in the simulation ($\Delta M = \dot{M} \times \Delta t$) in the limit as $\Delta t/t_{\text{Edd}}$ goes to zero (Volonteri et al. 2013). Given that the average SMBH time-step in ROMULUSC is at most $\sim 10^5$ yr (compared with $t_{\text{Edd}} \sim 5 \times 10^8$ yr) this is not a bad assumption to make. Nevertheless we confirm that our results remain the same were we to calculate t_{Edd} using $\langle \dot{M}_{\text{BH}} \rangle / \dot{M}_{\text{Edd}}$, averaged still over the previous 100 Myr and \dot{M}_{Edd} calculated using the black hole mass at the end of the time bin.

In Fig. 18 we see that at lower redshifts there is a dearth of actively growing SMBHs compared to the field that is especially drastic for lower mass galaxies. Looking out to higher redshift, the population of cluster SMBHs with the highest Eddington ratios become more similar to that of the field. Still, out to $z = 2$ we see there remains a much more significant population of SMBHs in cluster member galaxies that experience very little growth or none at all.

Observations of AGN in clusters, particularly those that are X-ray selected, generally can only pick out the highest accretion rates. We find that, while the distribution of Eddington ratios in cluster galaxies is significantly different from the field at all redshifts, the population of bright AGN may not show such a stark difference at all redshifts. In Fig. 19 we plot the fraction of galaxies hosting SMBHs that would result in luminous AGN as a function of galaxy

stellar mass for two bolometric luminosity thresholds similar to observational limits for AGN detection in the X-ray (e.g. Rosario et al. 2013, 2015). As with the average Eddington ratios, the average luminosity over the previous 100 Myr is used. At the highest redshifts, the population of luminous AGN is similar between the field and the cluster environments. At lower redshifts, the higher luminosity AGN remain mostly similar to the field, but the low-luminosity AGN population, particularly those in low-mass galaxies, becomes significantly lower in ROMULUSC.

5 DISCUSSION

5.1 The success of thermally coupled AGN feedback

The ability of a thermally coupled feedback prescription for SMBHs to create large-scale, *naturally collimated* winds is an important result of ROMULUSC with critical implications for the cosmological simulation community. It demonstrates that previous failures of thermal coupling of AGN feedback to limit star formation in massive galaxies, often used as justification for implementing more complicated mechanical feedback models (e.g. Ragono-Figueroa et al. 2013; Choi et al. 2015), are not intrinsic to thermal feedback. Rather, we argue that it is the result of limited resolution. With high resolution in mass, space, and time, we are able to more effectively model the interaction between the AGN and surrounding *nearby* gas because that gas is able to appropriately respond to the influx of thermal energy (in part due to our brief cooling shutoff). The inference that limited resolution leads to an overcooling of gas is not a new concept and has previously been examined in relation to stellar feedback (Katz 1992) and galaxy clusters (Lewis et al.

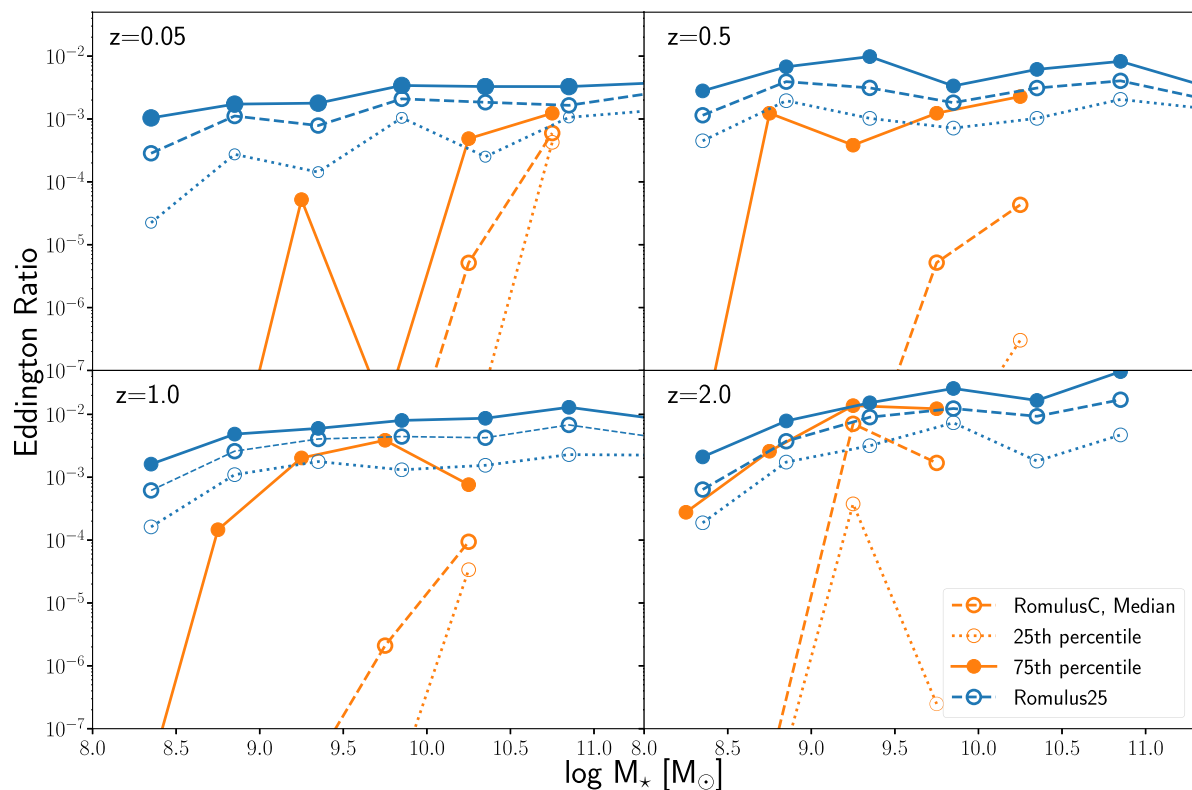


Figure 18. SMBH growth over cosmic time. The distribution of Eddington ratios for SMBHs in different environments. The 25th, 50th, and 75th percentiles are shown for SMBHs in different mass galaxies in high-density environments (ROMULUSC, orange) as well as relatively isolated galaxies in the field (ROMULU25, blue). In the cluster environment, there is a much more significant fraction of SMBHs that are growing at extremely low rates and in some cases not going at all. This occurs at all mass scales and at all redshifts. The highest Eddington ratio SMBHs are most similar between the different environments, especially at higher redshift.

2000), but ROMULUSC demonstrates that the solution to the problem for energy input from AGN does not have to lie in a kinetically coupled feedback (i.e. where particles are pushed rather than heated) or a very high coupling efficiency. This is not to say that there are not important physical motivations behind implementing kinetic or variable efficiency models (e.g. outflows and jets observed to exist in massive galaxies), but this must be properly separated from the issue of overcoming a numerical limitation.

The fact that the thermal feedback naturally forms collimated outflows is an interesting result. This is likely due to both the morphology of the gas near the SMBHs (the outflowing gas will take the path of least resistance) and the angular momentum of the gas that receives feedback and drives the base of the outflow. The transformation of an initially isotropic outflow into a collimated outflow on large scales is a well-studied phenomena. Various works on stellar winds have shown that when an initially isotropic outflow interacts with a medium with anisotropic density and pressure, it will elongate and form a jet-like structure along the steepest pressure gradient (Konigl 1982; Canto, Tenorio-Tagle & Rozyczka 1988; Raga & Canto 1989). As the jet propagates, it can remain collimated due to external pressure support when certain conditions are met in both the ambient medium and the velocity of the jet relative to its internal sound speed (Konigl 1982; Begelman, Blandford & Rees 1984). The jet-like structures we see in ROMULUSC are therefore the direct consequence of an initially spherical outflow interacting with the denser gas in the cluster core that has a disc morphology. Indeed when this structure is destroyed by the merger at $z \sim 0.2$, the black hole’s activity declines by almost two orders of magni-

tude and the bipolar outflows are no longer present. More idealized, high-resolution simulations of AGN feedback also have shown that a purely thermal model can drive asymmetric, large-scale outflows in Milky Way-mass galaxies (Gabor & Bournaud 2014).

It is important to note that our sub-grid models for stellar and SMBH physics have all been optimized based on reproducing empirical relations at Milky Way and dwarf mass scales. *The results presented in this work are therefore purely a prediction of our model and have been in no way constrained to produce a realistic BCG or ICM.* From this perspective, the results presented here from ROMULUSC reproduce many key observed properties of clusters and cluster galaxies is a significant success of our sub-grid model and our optimization process, but it also implies that the physics of star formation and, in particular, SMBHs, does not have to be particularly different in cluster environments, as it is in many other cosmological simulations through the implementation of ‘two-mode’ AGN feedback (e.g. Weinberger et al. 2017; Pillepich et al. 2018).

A logical next step in exploring the physics of AGN feedback would be to make the coupling and/or radiative efficiency variable over the lifetime of the SMBH. This would affect the overall balance between SMBH growth and feedback. For a higher efficiency, less accretion is required for the same energetic effect. Less accretion means that the SMBH grows less over time and that gas near the SMBH does not need to be as cool or dense and so there may also be less star formation. Possibly, the fact that we see a relatively high stellar mass in our BCG compared with observations is an indication that a more efficient feedback is required at high masses.

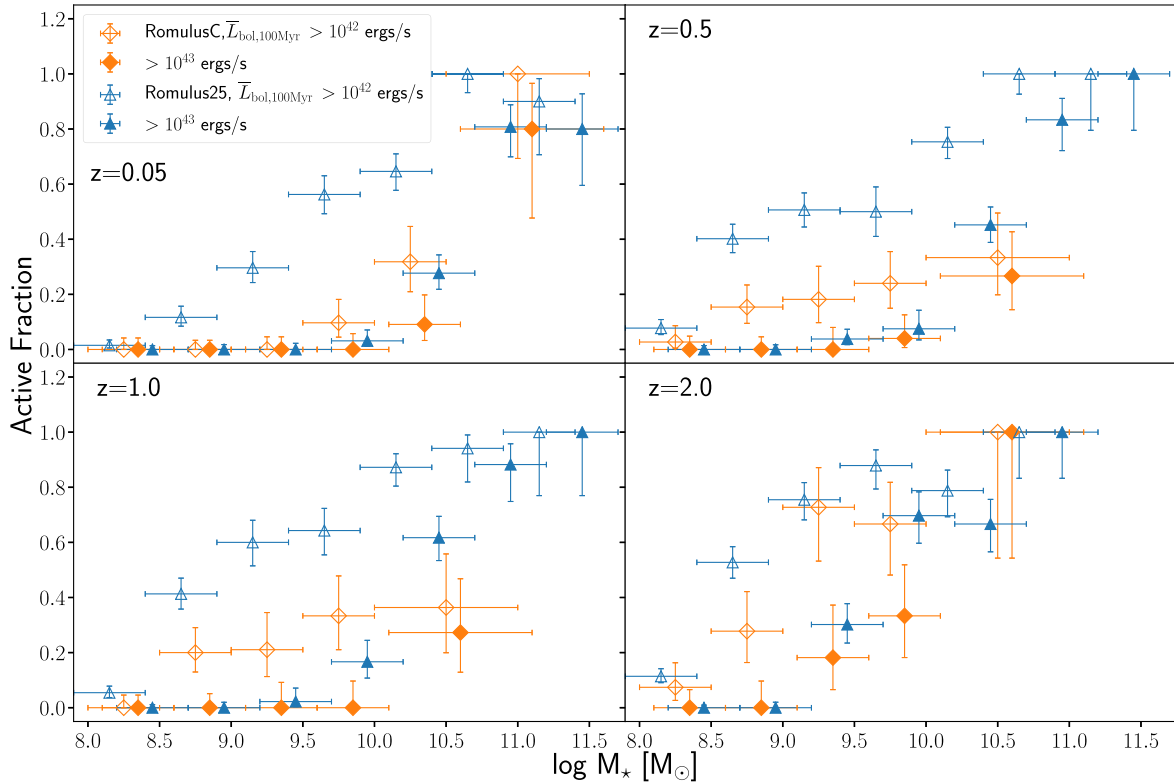


Figure 19. The population of luminous AGN. The fraction of galaxies hosting SMBHs that have a luminosity above a threshold of 10^{42} (open points) and 10^{43} (closed points) erg s^{-1} as a function of stellar mass at four different redshifts. Luminosities are averaged over the previous 100 Myr. Note that we do not include $z = 0$ because the black hole properties are only followed to $z = 0.05$ in ROMULUS25. Low-luminosity AGN are much more affected by their environment while high-luminosity AGN, which occur only in more massive galaxies, seem relatively insensitive to being in a cluster versus relatively isolated galaxy. Both AGN fractions evolve significantly with redshift such that, by $z = 2$, both are very similar to the field. This is in contrast with Fig. 18, which shows a substantial population of very low Eddington ratio SMBHs. When only focusing on high luminosity (which means high accretion rate) much of the difference in environment seen in the Eddington ratio vanishes, leading to claims that observed high-redshift AGN population in clusters are similar to or even enhanced compared with the field. Error bars represent the 68 per cent binomial confidence interval (Cameron 2011).

The final mass of the BCG’s central SMBH is $10^{10} M_{\odot}$, which is a factor of a few above the black hole mass stellar mass relation given our BCG’s stellar mass. While there is mounting observational evidence in support of overly massive black holes in BCGs and groups (e.g. McConnell & Ma 2013; Mezcua et al. 2018), this could be additional evidence that higher feedback efficiency is needed. Such a model could be justified by observations of different feedback mechanisms, such as jets and radio bubbles in the centres of clusters. However, there remains a lot of uncertainties and adopting such a model would require the addition of several free parameters.

As discussed in Section 2.1, ROMULUSC does not include metal line cooling, an important coolant for warm/hot ICM gas in the centres of massive haloes. This will affect the accretion history of the central galaxy in massive haloes. van de Voort et al. (2011b) show that metal line cooling will impact the accretion history of gas in the central galaxies hosted in the most massive haloes at both early and late times. However, AGN feedback also has a significant effect on gas inflow on to galaxies in massive haloes (van de Voort et al. 2011a,b). The relative roles of metal line cooling and AGN feedback in regulating the cooling of the ICM and star formation in the central galaxy is uncertain. Exploring this further will require simulations that self-consistently model the ISM and CGM/ICM with full metal line cooling and molecular hydrogen physics, as well as significantly higher resolution than even what we have attained with ROMULUSC.

5.2 Star formation in cluster member galaxies

The lack of star formation we see in cluster member galaxies is consistent with both observations (e.g. Drinkwater et al. 2001; van den Bosch et al. 2008; Weinmann et al. 2011; Haines et al. 2013, 2015; Boselli et al. 2014; Balogh et al. 2016; Bluck et al. 2016; Habas et al. 2018) as well as recent simulation work (e.g. Bahé & McCarthy 2015; Oman & Hudson 2016; Shao et al. 2018; Zinger et al. 2018). It is interesting that we do not see any radial dependence for low-mass galaxy quenching. This is however not very surprising. Observations of such low-mass galaxies are generally limited to only a few clusters in the local Universe. Weinmann et al. (2011) do find evidence of radial dependence for dwarf galaxy quenching in Virgo, which is somewhat similar in mass to ROMULUSC (Urban et al. 2011), but not in the more massive Perseus cluster. We do still find some evidence for radial dependence at the higher mass end of our low-mass bin ($10^9 < M_{\star} < 10^{9.7} M_{\odot}$, not plotted), but any such dependence seems to go away at the lowest masses, which are both hard to observe and dominate our low-mass bin shown in Fig. 15. Quenching rates that depend little on radial distance are consistent with theoretical results from Zinger et al. (2018), who find that the virial shock extends out to $2R_{200}$ and can cause significant ram pressure stripping of smaller galaxies even before they in-fall beyond R_{200} , in addition to pre-processing. While Bahé et al. (2017) also find significant quenching at low masses in the Eagle

simulation, they discuss how this might be a resolution effect, as they also see significant quenching of low-mass galaxies in lower density environments (Schaye et al. 2015) due to stellar feedback creating discs that are more unstable to stripping. As explored in Schaye et al. (2015), the quenching at the low-mass end is resolution dependent, but in the highest resolution EAGLE simulation, which is of similar resolution to ROMULUS, they find reasonable quenched fractions down to stellar masses of $10^8 M_{\odot}$, as we find for isolated field dwarfs in ROMULUS25 (see Fig. 14).

Analysis of cluster galaxies in the Virgo cluster by Boselli et al. (2014) indicate that at lower masses ram pressure stripping is likely the dominant source of quenching in the inner regions of the halo. Zinger et al. (2018) show that although ram pressure is crucial in stripping away hot halo gas even at large radii, much closer approaches to the cluster core are required to destroy star forming discs. This process often leads to strangulation of star formation by stripping away the supply of gas from galaxies but not directly destroying their discs. However, it has been shown that the inclusion of feedback processes, which in isolation create galactic outflows and fountains, make ram pressure more effective by making the ISM more susceptible to being stripped (Murakami & Babul 1999; Bahé & McCarthy 2015). Thus, it is not surprising that we see an enhanced quenched population of low-mass galaxies extending out to large radii.

This picture of ram pressure-dominated quenching is also consistent with our result that more massive galaxies tend to quench after falling closer to the cluster centre. Ram pressure stripping will be less efficient in these galaxies due to their deeper potential well and massive gaseous disc. Feedback processes that can enhance this stripping are also less effective for the same reason and so higher amounts of ram pressure are needed to destroy the gaseous disc. It is also possible that this difference is due to a combination of ram pressure stripping taking longer in more massive galaxies and shorter orbital decay time-scales for more massive sub-haloes. We will conduct a more detailed analysis relating ram pressure to both star formation and SMBH activity (see Sections 4.2.3 and 5.3).

The majority (71 per cent) of the galaxies that quench beyond R_{200} in ROMULUSC have been pre-processed as satellites of another in-falling halo. Such pre-processing has been used to explain observations of quenched galaxies at large cluster-centric radii (Fujita 2004; Haines et al. 2015). Still, a significant fraction of these quenched galaxies in ROMULUSC that quench far from the cluster centre have never been within R_{200} of another galaxy, including the main halo (i.e. they are not backsplash galaxies). This could imply that cluster galaxies can experience unique interactions with their environment without requiring them to be a satellite prior to cluster infall, as shown in previous simulations (Bahé et al. 2013; Zinger et al. 2018).

5.3 AGN activity in cluster member galaxies

Like star formation, we find that SMBH activity is significantly decreased in cluster environments, in agreement with low-redshift observations of luminous AGN in clusters compared to the field (Haines et al. 2012; Ehlert et al. 2013, 2014). The fact that only the most massive cluster galaxies host more luminous AGN with high accretion rates at lower redshift is also consistent with observations (Pimblet et al. 2013). Observations have also indicated that the AGN population in clusters evolves significantly with redshift, eventually meeting or even surpassing the AGN fractions in the field (Lehmer et al. 2013; Martini et al. 2013). ROMULUSC also shows a significant evolution with redshift, where higher luminosity, higher Eddington ratio AGN become more common at all masses out to $z =$

2. Importantly, while the fraction of luminous AGN in cluster galaxies matches closely with the field values at $z = 2$, consistent with observed clusters, it is clear that looking only at the SMBHs with the highest accretion rates does not give the full picture. Rather, we predict a much more substantial population of extremely low Eddington ratio (or even completely dormant) SMBHs in the cluster environment at all stellar masses and redshifts. This population will not be observed in most AGN surveys, which will generally be limited to sources with higher accretion rates. One potential way to distinguish this affect is to examine the dynamics of galaxies hosting AGN. Haines et al. (2012) show that luminous AGN in clusters tend to reside in in-falling galaxies, indicating that SMBH activity does indeed decline as the galaxies interact with the ICM.

It is important to note that with our limited volume and only a single cluster we do not completely sample the rarer, much higher luminosity SMBH growth events ($L_{\text{bol}} > 10^{44} \text{ erg s}^{-1}$). However, our results indicate that the picture of how the cluster environment affects SMBH growth may be quite different if one only focuses on high-luminosity AGN compared with the much more common low and intermediate luminosity sources. The fact that we find the brightest AGN mostly in higher mass galaxies indicates that the extent to which ram pressure has been able to strip the galaxy's gas supply may be the deciding factor. It may also be possible that ram pressure can drive some SMBH activity in these higher mass galaxies (Poggianti et al. 2017; Marshall et al. 2018). We will examine the connection between SMBH activity, galaxy gas supply, and ram pressure stripping in more detail in future work.

6 SUMMARY

We have presented first results from ROMULUSC, the highest resolution cosmological simulation of a galaxy cluster to date. The simulation is able to resolve cluster member galaxies with unprecedented detail down to dwarf galaxy mass scales. With a novel approach to SMBH physics (Tremmel et al. 2015, 2017) and spatial resolution of the order of 100 pc, ROMULUSC is able to resolve the internal processes of galaxies from cluster dwarfs to BCGs with unprecedented detail. While ROMULUSC lacks metal line cooling, as discussed in Sections 2.2.4 and 5.1 this choice was made based on previous studies demonstrating the problems with including it in simulations that are unable to resolve multiphase gas. This should be considered a limitation of our model to the same extent as including metal line cooling without the necessary resolution should be considered a limitation in other (generally lower resolution) simulations. Further, ROMULUSC represents an important test to our sub-grid models, particularly those related to SMBH growth and feedback, as they have only been optimized to produce realistic galaxies for haloes 100 times smaller than the main halo of ROMULUSC. We demonstrate that ROMULUSC is consistent with observations in terms of baryonic content, bulk properties, and structure of the ICM, stellar mass, and star formation history of the BCG, and quenched fractions for higher mass cluster member galaxies.

We show that the central BCG in ROMULUSC has a star formation history consistent with the average sSFR of BCGs observed out to high redshift, finding that local maxima and minima in the star formation history are closely associated with lower and higher levels of SMBH activity, respectively. Large-scale, collimated outflows are ubiquitous throughout the simulation and the longest period of sustained SMBH activity (8–10 Gyr) is associated with the final quenching of star formation in the BCG as well as particularly powerful outflows. The final stellar mass of the BCG is within a factor of 2 of the median of the stellar masses observed in similar mass haloes. Importantly, the large-scale outflows that are critical

to this quenching co-exist with a low-entropy core that maintains a short (<1 Gyr) cooling time. The effect of the AGN feedback is to limit the ability for halo gas to cool on to the central galaxy, rather than directly heat the gas to high temperatures (and entropy) or blow it away (e.g. McCarthy et al. 2011; Pontzen et al. 2017).

The fact that a simple AGN feedback model with thermally coupled, isotropic energy injection is able to drive powerful outflows that are *naturally* collimated in morphology is a major success and demonstrates that the failure of thermal AGN sub-grid feedback prescriptions have been limited not by inherent physics, but by poor resolution in time, space, and mass. The strength of this simple approach is that the large-scale nature of the outflows are purely a prediction of the model and not something placed by hand in the simulation through explicit kinetic feedback. The model also does not assume any characteristic mass scale at which different feedback modes become dominant. The motions of gas are driven by both local morphology (i.e. the morphology and angular momentum of the gas in the centre of the cluster) as well as larger scale cluster ‘weather’ driven by cluster galaxies and overall turbulence in the ICM. Our approach does include a (brief) cooling shutoff for gas that receives feedback in order to avoid any spurious overcooling. While this is physically motivated by the fact that feedback does not occur instantaneously, higher resolution simulations are still needed to self-consistently model the coupling of AGN feedback to gas on 100 pc scales. The high BCG stellar mass and black hole mass in ROMULUSC might be indicative that a higher feedback efficiency is required for SMBHs, a natural consequence if, as observations indicate, additional physical processes such as coupling to AGN jets are occurring on small scales preferentially for more massive galaxies/SMBHs.

Beyond the BCG and its central SMBH, we examine the evolving population of cluster member galaxies. We demonstrate the success of both ROMULUSC and our uniform volume simulation, ROMULUS25, in reproducing the observed fraction of quenched galaxies as a function of stellar mass in cluster environments and the field, respectively. Taking advantages of the high resolution of ROMULUSC we predict that 80–100 per cent of low mass ($M_* < 10^{10} M_\odot$) galaxies are quenched at $z = 0$ regardless of stellar mass or distance from the cluster centre, a fraction that is more than 10 times higher than that of isolated galaxies that almost never quench at low mass. More massive quenched galaxies in ROMULUSC have orbits that have taken them systematically closer ($D_{\min} \sim 0.4 R_{200}$) to the cluster centre prior to quenching while less massive galaxies tend to quench farther out ($D_{\min} \sim 0.6 R_{200}$). A significant fraction of galaxies (~ 25 per cent) quench before falling beyond R_{200} and 71 per cent of these galaxies have previously been satellites of another in-falling galaxy. This means that ~ 7 per cent of cluster galaxies quench beyond R_{200} yet have not been pre-processed as a satellite of another halo. These galaxies may have been quenched by the larger-scale cluster environment, consistent with results from Zinger et al. (2018). The enhanced fraction of quenched galaxies is in place even at $z = 2$ within $2R_{200}$ at all but the very highest masses.

Finally, we examine the population of SMBHs in ROMULUSC and find that overall SMBH growth is significantly suppressed in the cluster environment at all masses and redshifts. While the population of the highest Eddington ratio SMBHs, particularly those in more massive galaxies, become closer to field SMBHs at higher redshifts, the distribution of Eddington ratios in the cluster environment remains quite different. Thus, we predict, consistent with observations, that the most luminous AGN population evolves significantly with redshift and by $z = 2$ even relatively low-luminosity AGN ($L_{\text{bol}} > 10^{42} \text{ erg s}^{-1}$) become similar to the field. The population of AGN

most affected by the cluster environment is low-luminosity AGN, which are generally missed in observational studies of AGN.

7 FUTURE WORK AND SIMULATIONS

As mentioned throughout the paper, significant follow-up analysis is planned to better understand the detailed consequences of ram pressure stripping and pre-processing on star formation and SMBH accretion in cluster member galaxies. Also, a more detailed analysis of the structure and evolution of AGN winds and how they affect star formation and cooling in the BCG will take place in future work. The nature of SPH allows us to easily track the evolution of gas that directly receives AGN feedback and that which becomes entrained in large-scale winds, allowing us to better understand the morphology of these outflows and why star formation shuts off when it does.

ROMULUSC is the first of a planned suite of zoom-in simulations of massive haloes. Currently, we have several more zoom-in simulations planned including group-scale haloes ($M_{200} = 3\text{--}5 \times 10^{13} M_\odot$) as well as more massive clusters ($M_{200} = 2 \times 10^{14}\text{--}1 \times 10^{15} M_\odot$). These simulations, combined with the small galaxy groups in ROMULUSC ($M_{200} \sim 10^{12.5\text{--}13} M_\odot$) will allow us to further explore galaxy evolution and SMBH feedback in different environments and in the most massive galaxies. The success of our fiducial simulation that we present here is very encouraging and indicates that our sub-grid physics implementations are very much up to the task of modelling galaxy and SMBH evolution correctly within these unique environments.

ACKNOWLEDGEMENTS

The authors thank the anonymous referee for their careful reading and useful comments and suggestions for this manuscript. MT gratefully acknowledges support from the Yale Center for Astronomy and Astrophysics Prize Postdoctoral Fellowship. AB, TQ, and MT were partially supported by National Science Foundation award AST-1514868. AR acknowledges support from NASA Headquarters under the NASA Earth and Space Science Fellowship Program Grant 80NSSC17K0459. PN acknowledges useful discussions in her weekly research group meeting. AP is supported by the Royal Society. MV acknowledges funding from the European Research Council under the European Community’s Seventh Framework Programme (FP7/2007-2013 Grant Agreement no. 614199, project ‘BLACK’). This work is supported in part by National Science Foundation grant AST-141276 and the UCL Cosmoparticle Initiative. This research is part of the Blue Waters sustained-petascale computing project, which is supported by the National Science Foundation (awards OCI-0725070 and ACI-1238993) and the state of Illinois. Blue Waters is a joint effort of the University of Illinois at Urbana-Champaign and its National Center for Supercomputing Applications. This work is also part of a Petascale Computing Resource Allocations allocation support by the National Science Foundation (award number OAC-1613674). The analysis presented in this paper was done using the publicly available software packages, PYNBODY (Pontzen et al. 2013) and TANGOS (Pontzen & Tremmel 2018).

REFERENCES

- Andrade-Santos F. et al., 2017, *ApJ*, 843, 76
 Arnaud M., Pratt G. W., Piffaretti R., Böhringer H., Croston J. H., Pointecouteau E., 2010, *A&A*, 517, A92
 Babul A., Balogh M. L., Lewis G. F., Poole G. B., 2002, *MNRAS*, 330, 329

- Babul A., Sharma P., Reynolds C. S., 2013, *ApJ*, 768, 11
- Bahé Y. M., McCarthy I. G., 2015, *MNRAS*, 447, 969
- Bahé Y. M., McCarthy I. G., Balogh M. L., Font A. S., 2013, *MNRAS*, 430, 3017
- Bahé Y. M. et al., 2017, *MNRAS*, 470, 4186
- Balogh M. L., Babul A., Patton D. R., 1999, *MNRAS*, 307, 463
- Balogh M. L., Mazzotta P., Bower R. G., Eke V., Bourdin H., Lu T., Theuns T., 2011, *MNRAS*, 412, 947
- Balogh M. L. et al., 2016, *MNRAS*, 456, 4364
- Barnes D. J. et al., 2017a, *MNRAS*, 471, 1088
- Barnes D. J., Kay S. T., Henson M. A., McCarthy I. G., Schaye J., Jenkins A., 2017b, *MNRAS*, 465, 213
- Beckmann R. S. et al., 2017, *MNRAS*, 472, 949
- Begelman M. C., Blandford R. D., Rees M. J., 1984, *Rev. Mod. Phys.*, 56, 255
- Bildfell C., Hoekstra H., Babul A., Mahdavi A., 2008, *MNRAS*, 389, 1637
- Birzan L., McNamara B. R., Nulsen P. E. J., Carilli C. L., Wise M. W., 2008, *ApJ*, 686, 859
- Blanton E. L., Sarazin C. L., McNamara B. R., Wise M. W., 2001, *ApJ*, 558, L15
- Bluck A. F. L. et al., 2016, *MNRAS*, 462, 2559
- Bocquet S., Saro A., Dolag K., Mohr J. J., 2016, *MNRAS*, 456, 2361
- Boehringer H., Voges W., Fabian A. C., Edge A. C., Neumann D. M., 1993, *MNRAS*, 264, L25
- Bogdán Á., Lovisari L., Volonteri M., Dubois Y., 2018, *ApJ*, 852, 131
- Bonaventura N. R. et al., 2017, *MNRAS*, 469, 1259
- Booth C. M., Schaye J., 2009, *MNRAS*, 398, 53
- Boselli A. et al., 2014, *A&A*, 570, A69
- Bradford J. D., Geha M. C., Greene J. E., Reines A. E., Dickey C. M., 2018, *ApJ*, 861, 50
- Bromm V., Loeb A., 2003, *ApJ*, 596, 34
- Cameron E., 2011, *Publ. Astron. Soc. Aust.*, 28, 128
- Canto J., Tenorio-Tagle G., Rozyczka M., 1988, *A&A*, 192, 287
- Choi E., Ostriker J. P., Naab T., Oser L., Moster B. P., 2015, *MNRAS*, 449, 4105
- Christensen C. R., Governato F., Quinn T., Brooks A. M., Shen S., McCleary J., Fisher D. B., Wadsley J., 2014, *MNRAS*, 440, 2843
- Chung A., van Gorkom J. H., Kenney J. D. P., Vollmer B., 2007, *ApJ*, 659, L115
- Cielo S., Antonuccio-Delogu V., Macciò A. V., Romeo A. D., Silk J., 2014, *MNRAS*, 439, 2903
- Cielo S., Antonuccio-Delogu V., Silk J., Romeo A. D., 2017, *MNRAS*, 467, 4526
- Cielo S., Babul A., Antonuccio-Delogu V., Silk J., Volonteri M., 2018a, *A&A*, 617, A58
- Cielo S., Bieri R., Volonteri M., Wagner A. Y., Dubois Y., 2018b, *MNRAS*, 477, 1336
- Croston J. H., Hardcastle M. J., Mingo B., Evans D. A., Dicken D., Morganti R., Tadhunter C. N., 2011, *ApJ*, 734, L28
- Dalla Vecchia C., Schaye J., 2012, *MNRAS*, 426, 140
- De Young D. S., 2006, *ApJ*, 648, 200
- DeMaio T., Gonzalez A. H., Zabludoff A., Zaritsky D., Connor T., Donahue M., Mulchaey J. S., 2018, *MNRAS*, 474, 3009
- Di Cintio A., Tremmel M., Governato F., Pontzen A., Zavala J., Bastidas Fry A., Brooks A., Vogelsberger M., 2017, *MNRAS*, 469, 2845
- Di Matteo T., Springel V., Hernquist L., 2005, *Nature*, 433, 604
- Di Matteo T., Colberg J., Springel V., Hernquist L., Sijacki D., 2008, *ApJ*, 676, 33
- Dolag K., Komatsu E., Sunyaev R., 2016, *MNRAS*, 463, 1797
- Drinkwater M. J., Gregg M. D., Holman B. A., Brown M. J. I., 2001, *MNRAS*, 326, 1076
- Dubois Y., Devriendt J., Slyz A., Teyssier R., 2012, *MNRAS*, 420, 2662
- Dubois Y. et al., 2014, *MNRAS*, 444, 1453
- Dunn R. J. H., Fabian A. C., 2006, *MNRAS*, 373, 959
- Ehler S. et al., 2014, *MNRAS*, 437, 1942
- Ehler S., Allen S. W., Brandt W. N., Xue Y. Q., Luo B., von der Linden A., Mantz A., Morris R. G., 2013, *MNRAS*, 428, 3509
- Elahi P. J. et al., 2016, *MNRAS*, 458, 1096
- Fabian A. C., 1994, *ARA&A*, 32, 277
- Fabian A. C., Celotti A., Blundell K. M., Kassim N. E., Perley R. A., 2002, *MNRAS*, 331, 369
- Fujita Y., 2004, *PASJ*, 56, 29
- Gabor J. M., Bournaud F., 2014, *MNRAS*, 441, 1615
- Gaspari M., Sądowski A., 2017, *ApJ*, 837, 149
- Gaspari M., Brighenti F., Temi P., 2012, *MNRAS*, 424, 190
- Gaspari M., Churazov E., Nagai D., Lau E. T., Zhuravleva I., 2014, *A&A*, 569, A67
- Geha M., Blanton M. R., Yan R., Tinker J. L., 2012, *ApJ*, 757, 85
- Genel S. et al., 2014, *MNRAS*, 445, 175
- Gonzalez A. H., Sivanandam S., Zabludoff A. I., Zaritsky D., 2013, *ApJ*, 778, 14
- Governato F. et al., 2015, *MNRAS*, 448, 792
- Guedes J., Callegari S., Madau P., Mayer L., 2011, *ApJ*, 742, 76
- Guo F., Duan X., Yuan Y. F., 2018, *MNRAS*, 473, 1332
- Habas R., Fadda D., Marleau F. R., Biviano A., Durret F., 2018, *MNRAS*, 475, 4544
- Haines C. P. et al., 2012, *ApJ*, 754, 97
- Haines C. P. et al., 2013, *ApJ*, 775, 126
- Haines C. P. et al., 2015, *ApJ*, 806, 101
- Hardcastle M. J., Croston J. H., 2010, *MNRAS*, 404, 2018
- Hardcastle M. J., Sakelliou I., Worrall D. M., 2005, *MNRAS*, 359, 1007
- Heinz S., Brügggen M., Young A., Levesque E., 2006, *MNRAS*, 373, L65
- Hester J. A., 2006, *ApJ*, 647, 910
- Hitomi Collaboration, 2016, *Nature*, 535, 117
- Hoekstra H., Herbonnet R., Muzzin A., Babul A., Mahdavi A., Viola M., Cacciato M., 2015, *MNRAS*, 449, 685
- Jauzac M. et al., 2015, *MNRAS*, 452, 1437
- Katz N., 1992, *ApJ*, 391, 502
- Katz N., White S. D. M., 1993, *ApJ*, 412, 455
- Knollmann S. R., Knebe A., 2009, *ApJ*, 182, 608
- Konigl A., 1982, *ApJ*, 261, 115
- Kravtsov A. V., Vikhlinin A., Meshcheryakov A. V., 2018, *Astron. Lett.*, 44, 8
- Kroupa P., 2001, *MNRAS*, 322, 231
- Laganá T. F., Martinet N., Durret F., Lima Neto G. B., Maughan B., Zhang Y.-Y., 2013, *A&A*, 555, A66
- Lau E. T., Gaspari M., Nagai D., Coppi P., 2017, *ApJ*, 849, 54
- Lehmer B. D. et al., 2013, *ApJ*, 765, 87
- Lewis G. F., Babul A., Katz N., Quinn T., Hernquist L., Weinberg D. H., 2000, *ApJ*, 536, 623
- Li Y., Bryan G. L., 2014, *ApJ*, 789, 54
- Li Y., Bryan G. L., Ruszkowski M., Voit G. M., O'Shea B. W., Donahue M., 2015, *ApJ*, 811, 73
- Li Y., Ruszkowski M., Bryan G. L., 2017, *ApJ*, 847, 106
- Liang L., Durier F., Babul A., Davé R., Oppenheimer B. D., Katz N., Fardal M., Quinn T., 2016, *MNRAS*, 456, 4266
- Lin Y. T., Mohr J. J., Stanford S. A., 2003, *ApJ*, 591, 749
- Lodato G., Natarajan P., 2006, *MNRAS*, 371, 1813
- Lotz M., Remus R.-S., Dolag K., Biviano A., Burkert A., 2018, preprint ([arXiv:1810.02382](https://arxiv.org/abs/1810.02382))
- Loubser S. I., Babul A., Hoekstra H., Mahdavi A., Donahue M., Bildfell C., Voit G. M., 2016, *MNRAS*, 456, 1565
- Mahdavi A., Hoekstra H., Babul A., Henry J. P., 2008, *MNRAS*, 384, 1567
- Mahdavi A., Hoekstra H., Babul A., Bildfell C., Jeltema T., Henry J. P., 2013, *ApJ*, 767, 116
- Maier C. et al., 2016, *A&A*, 590, A108
- Marinacci F. et al., 2018, *MNRAS*, 480, 5113
- Marshall M. A., Shabala S. S., Krause M. G. H., Pimblett K. A., Croton D. J., Owers M. S., 2018, *MNRAS*, 474, 3615
- Martini P. et al., 2013, *ApJ*, 768, 1
- Mazzotta P., Rasia E., Moscardini L., Tormen G., 2004, *MNRAS*, 354, 10
- McCarthy I. G., Babul A., Bower R. G., Balogh M. L., 2008, *MNRAS*, 386, 1309
- McCarthy I. G., Schaye J., Bower R. G., Ponman T. J., Booth C. M., Dalla Vecchia C., Springel V., 2011, *MNRAS*, 412, 1965
- McCarthy I. G., Schaye J., Bird S., Le Brun A. M. C., 2017, *MNRAS*, 465, 2936
- McConnell N. J., Ma C. P., 2013, *ApJ*, 764, 184

- McDonald M. et al., 2013, *ApJ*, 774, 23
- McDonald M. et al., 2014, *ApJ*, 794, 67
- McDonald M. et al., 2016, *ApJ*, 817, 86
- McDonald M. et al., 2017, *ApJ*, 843, 28
- McNamara B. R., Nulsen P. E. J., 2012, *New J. Phys.*, 14, 55023
- McNamara B. R. et al., 2000, *ApJ*, 534, L135
- McNamara B. R., Kazemzadeh F., Rafferty D. A., Bîrzan L., Nulsen P. E. J., Kirkpatrick C. C., Wise M. W., 2009, *ApJ*, 698, 594
- Mendygral P. J., Jones T. W., Dolag K., 2012, *ApJ*, 750, 166
- Menon H., Wesolowski L., Zheng G., Jetley P., Kale L., Quinn T., Governato F., 2015, *Comput. Astrophys. Cosmol.*, 2, 1
- Merluzzi P. et al., 2013, *MNRAS*, 429, 1747
- Mezcua M., Hlavacek-Larrondo J., Lucey J. R., Hogan M. T., Edge A. C., McNamara B. R., 2018, *MNRAS*, 474, 1342
- Mistani P. A. et al., 2016, *MNRAS*, 455, 2323
- Mittal R., Hudson D. S., Reiprich T. H., Clarke T., 2009, *A&A*, 501, 835
- Moore B., Katz N., Lake G., Dressler A., Oemler A., 1996, *Nature*, 379, 613
- Moore B., Lake G., Katz N., 1998, *ApJ*, 495, 139
- Moore B., Lake G., Quinn T., Stadel J., 1999, *MNRAS*, 304, 465
- Morsony B. J., Heinz S., Brügggen M., Ruzzkowski M., 2010, *MNRAS*, 407, 1277
- Munshi F. et al., 2013, *ApJ*, 766, 56
- Murakami I., Babul A., 1999, *MNRAS*, 309, 161
- Nagai D., Kravtsov A. V., Vikhlinin A., 2007, *ApJ*, 668, 1
- Nagai D., Vikhlinin A., Kravtsov A. V., 2007, *ApJ*, 655, 98
- Natarajan P., Kneib J.-P., Smail I., Treu T., Ellis R., Moran S., Limousin M., Czoske O., 2009, *ApJ*, 693, 970
- Nelson K., Lau E. T., Nagai D., 2014, *ApJ*, 792, 25
- O'Neill S. M., Jones T. W., 2010, *ApJ*, 710, 180
- O'Sullivan E. et al., 2012, *MNRAS*, 424, 2971
- Oman K. A., Hudson M. J., 2016, *MNRAS*, 463, 3083
- Peterson J. R., Fabian A. C., 2006, *Phys. Rep.*, 427, 1
- Pillepich A. et al., 2018, *MNRAS*, 475, 648
- Pimblett K. A., Shabala S. S., Haines C. P., Fraser-McKelvie A., Floyd D. J. E., 2013, *MNRAS*, 429, 1827
- Planck Collaboration XIII 2016, *A&A*, 594, A13
- Poggianti B. M. et al., 2017, *Nature*, 548, 304
- Pontzen A., Tremmel M., 2018, *ApJS*, 237, 23
- Pontzen A. et al., 2008, *MNRAS*, 390, 1349
- Pontzen A., Roškar R., Stinson G., Woods R., 2013, pynbody: N-Body/SPH analysis for python. Astrophysics Source Code Library. record ascl:1305.002
- Pontzen A., Tremmel M., Roth N., Peiris H. V., Saintonge A., Volonteri M., Quinn T., Governato F., 2017, *MNRAS*, 465, 547
- Poole G. B., Fardal M. A., Babul A., McCarthy I. G., Quinn T., Wadsley J., 2006, *MNRAS*, 373, 881
- Poole G. B., Babul A., McCarthy I. G., Sanderson A. J. R., Fardal M. A., 2008, *MNRAS*, 391, 1163
- Power C., Navarro J. F., Jenkins A., Frenk C. S., White S. D. M., Springel V., Stadel J., Quinn T., 2003, *MNRAS*, 338, 14
- Prasad D., Sharma P., Babul A., 2015, *ApJ*, 811, 108
- Prasad D., Sharma P., Babul A., 2017, *MNRAS*, 471, 1531
- Prasad D., Sharma P., Babul A., 2018, *ApJ*, 863, 62
- Rafferty D. A., McNamara B. R., Nulsen P. E. J., Wise M. W., 2006, *ApJ*, 652, 216
- Raga A. C., Canto J., 1989, *ApJ*, 344, 404
- Ragone-Figueroa C., Granato G. L., Murante G., Borgani S., Cui W., 2013, *MNRAS*, 436, 1750
- Ragone-Figueroa C., Granato G. L., Ferraro M. E., Murante G., Biffi V., Borgani S., Planelles S., Rasia E., 2018, *MNRAS*, 479, 1125
- Ritchie B. W., Thomas P. A., 2001, *MNRAS*, 323, 743
- Roediger E. et al., 2015, *ApJ*, 806, 104
- Roediger J. C. et al., 2017, *ApJ*, 836, 120
- Rosario D. J. et al., 2013, *ApJ*, 763, 59
- Rosario D. J. et al., 2015, *A&A*, 573, A85
- Ruzzkowski M., Oh S. P., 2010, *ApJ*, 713, 1332
- Sanderson A. J. R., O'Sullivan E., Ponman T. J., 2009, *MNRAS*, 395, 764
- Schaye J. et al., 2015, *MNRAS*, 446, 521
- Schneider R., Ferrara A., Natarajan P., Omukai K., 2002, *ApJ*, 571, 30
- Shao S., Cautun M., Deason A. J., Frenk C. S., Theuns T., 2018, *MNRAS*, 479, 284
- Shen S., Wadsley J., Stinson G., 2010, *MNRAS*, 407, 1581
- Shen S., Madau P., Aguirre A., Guedes J., Mayer L., Wadsley J., 2012, *ApJ*, 760, 50
- Shirasaki M., Lau E. T., Nagai D., 2017, *MNRAS*, 477, 2804
- Sijacki D., Springel V., Di Matteo T., Hernquist L., 2007, *MNRAS*, 380, 877
- Sijacki D., Vogelsberger M., Genel S., Springel V., Torrey P., Snyder G. F., Nelson D., Hernquist L., 2015, *MNRAS*, 452, 575
- Smith G. P. et al., 2010, *A&A*, 518, L18
- Smith G. P. et al., 2016, *MNRAS*, 456, L74
- Snios B. et al., 2018, *ApJ*, 855, 71
- Soker N., Bisker G., 2006, *MNRAS*, 369, 1115
- Sokolowska A., Mayer L., Babul A., Madau P., Shen S., 2016, *ApJ*, 819, 21
- Sokolowska A., Babul A., Mayer L., Shen S., Madau P., 2018, *ApJ*, 867, 73
- Springel V., Di Matteo T., Hernquist L., 2005, *ApJ*, 620, L79
- Stinson G., Seth A., Katz N., Wadsley J., Governato F., Quinn T., 2006, *MNRAS*, 373, 1074
- Sun M., Voit G. M., Donahue M., Jones C., Forman W., Vikhlinin A., 2009, *ApJ*, 693, 1142
- Teyssier R., Moore B., Martizzi D., Dubois Y., Mayer L., 2011, *MNRAS*, 414, 195
- Tremmel M., Governato F., Volonteri M., Quinn T. R., 2015, *MNRAS*, 451, 1868
- Tremmel M., Karcher M., Governato F., Volonteri M., Quinn T. R., Pontzen A., Anderson L., Bellovary J., 2017, *MNRAS*, 470, 1121
- Tremmel M., Governato F., Volonteri M., Pontzen A., Quinn T. R., 2018, *ApJ*, 857, L22
- Tremmel M., Governato F., Volonteri M., Quinn T. R., Pontzen A., 2018, *MNRAS*, 475, 4967
- Urban O., Werner N., Simionescu A., Allen S. W., Böhringer H., 2011, *MNRAS*, 414, 2101
- van de Voort F., Schaye J., Booth C. M., Dalla Vecchia C., 2011a, *MNRAS*, 415, 2782
- van de Voort F., Schaye J., Booth C. M., Haas M. R., Dalla Vecchia C., 2011b, *MNRAS*, 414, 2458
- van den Bosch F. C., Aquino D., Yang X., Mo H. J., Pasquali A., McIntosh D. H., Weinmann S. M., Kang X., 2008, *MNRAS*, 387, 79
- Vernaleo J. C., Reynolds C. S., 2006, *ApJ*, 645, 83
- Vikhlinin A., 2006, *ApJ*, 640, 710
- Vogelsberger M., Genel S., Sijacki D., Torrey P., Springel V., Hernquist L., 2013, *MNRAS*, 436, 3031
- Volonteri M., Sikora M., Lasota J.-P., Merloni A., 2013, *ApJ*, 775, 94
- Wadsley J. W., Stadel J., Quinn T., 2004, *New Astron.*, 9, 137
- Wadsley J. W., Veeravalli G., Couchman H. M. P., 2008, *MNRAS*, 387, 427
- Wadsley J. W., Keller B. W., Quinn T. R., 2017, *MNRAS*, 471, 2357
- Weinberger R. et al., 2017, *MNRAS*, 465, 3291
- Weinmann S. M., van den Bosch F. C., Yang X., Mo H. J., 2006, *MNRAS*, 366, 2
- Weinmann S. M., Lisker T., Guo Q., Meyer H. T., Janz J., 2011, *MNRAS*, 416, 1197
- Wetzel A. R., Tinker J. L., Conroy C., 2012, *MNRAS*, 424, 232
- Wetzel A. R., Tinker J. L., Conroy C., van den Bosch F. C., 2013, *MNRAS*, 432, 336
- Whitaker K. E. et al., 2011, *ApJ*, 735, 86
- Wu H.-Y., Evrard A. E., Hahn O., Martizzi D., Teyssier R., Wechsler R. H., 2015, *MNRAS*, 452, 1982
- Yang H. Y. K., Reynolds C. S., 2016, *ApJ*, 829, 90
- Zhang Y.-Y. et al., 2010, *ApJ*, 711, 1033
- Zhuravleva I., Churazov E., Kravtsov A., Lau E. T., Nagai D., Sunyaev R., 2013, *MNRAS*, 428, 3274
- Zinger E., Dekel A., Kravtsov A. V., Nagai D., 2018, *MNRAS*, 475, 3654

This paper has been typeset from a $\text{\TeX}/\text{\LaTeX}$ file prepared by the author.